THE ASTROPHYSICAL JOURNAL, 302:208–233, 1986 March 1

INTERNAL KINEMATICS OF SPIRAL GALAXIES: GAS AND STELLAR ROTATION CURVES AND DISPERSION PROFILES

JAMES A. FILLMORE
Astronomy Department, California Institute of Technology
TODD A. BOROSON[1]
Mount Wilson and Las Campanas Observatories, Carnegie Institution of Washington, and Astronomy Department, University of Michigan
AND
ALAN DRESSLER[1]
Mount Wilson and Las Campanas Observatories, Carnegie Institution of Washington

Received 1985 February 14; accepted 1985 September 3

ABSTRACT

We present emission- and absorption-line observations of six moderately inclined spiral galaxies. The mean rotation and velocity dispersion for the gas and the stars have been measured. Two component mass models are fitted to surface brightness measurements and are used to fit kinematic models to the velocity data. Models with constant mass-to-light ratios and isotropic velocity dispersions roughly fit the inner regions of spiral galaxies with three caveats.

1. Several galaxies show significant kinematic differences between the two sides of the galaxy. While the differences might be caused by non-axisymmetric potentials, variations in the line-of-sight extinction are a more likely cause.
2. The inner portion ($R \leq 1$ kpc) of the emission-line (gas) rotation curve falls below the predicted circular velocity. Because the model circular velocities are computed from the observed stellar velocities, variations in the total mass-to-light ratio will not change the model values. We note that gas lost from bulge giants (planetary nebulae) will have a significant *noncircular* velocity component. We show that these emitted "clouds" live a sufficient time to explain the lower-than-circular velocity of the emission-line rotation curves.
3. Some of the bulges are flatter than one would expect from their rotation rate, assuming isotropic random motions, but this additional flattening could be caused by the disk potential.

Subject headings: galaxies: internal motions — galaxies: structure

I. INTRODUCTION

While much effort in recent years has been devoted to understanding rotation curves, studies have concentrated primarily on their behavior at large radii. The velocities of material at small radii are important, however, for determining the distribution of mass within galaxies, as well as the dynamical effects of the different galaxian components upon each other. For example, the questions which one might hope to address with high-resolution data on the inner regions of disk galaxies include the following: (1) Are bulges flattened by rotation or anisotropic residual velocities? (2) How do the bulge and disk interact? (3) How does the mass-to-light ratio (M/L) change with radius? This last question involves such aspects as how centrally concentrated a massive halo is and whether black holes are commonly found in the centers of galaxies.

Recent progress in both observational capabilities and theoretical models suggests that the time is now right to study inner rotation curves in some detail. The same advances in detector technology which allow the measurement of optical rotation curves at very large radii and, hence, very low surface brightnesses, enable the measurement of the inner parts of galaxy rotation curves at unprecedentedly high spatial and spectral resolution. Also, the advances made in modeling elliptical galaxies provide a good framework for studying the velocity and surface brightness distributions of spheroids within disk systems.

In this paper we present observations and analysis of velocity data from six spiral galaxies. These data consist of radial velocities and velocity dispersions of both the gaseous and the stellar components. The measurements extend out to several kiloparsecs, and the spatial resolution is limited by the seeing. The analysis utilizes all the velocity data, as well as light distributions for the galaxies, to model the mass distributions and the motions of the material in a nearly self-consistent way. Section II contains the details of the observations and the data reduction. Section III is an explanation of the modeling procedure. In § IV, this procedure is applied to each of the six galaxies observed. In § V, we discuss the trends and individual peculiarities and their implications for galaxy formation and evolution.

II. OBSERVATIONS AND REDUCTIONS

All the observations were made with the Double Spectrograph at the Cassegrain focus of the Hale 5 m telescope. A 320 × 512 RCA CCD was the detector on the blue side of the spectrograph, and an 800 × 800 TI CCD was the detector on the red side. All of the emission-line measurements were made in the λ6500–λ6800 region, which includes Hα, the [N II] $\lambda\lambda$6548, 6583 lines, and the [S II] $\lambda\lambda$6716, 6731 lines. The absorption-line measurements were made either in the λ4400–λ5400 region, which contains Hβ and the Mg I *b* feature, or in the λ8400–λ8700 region, which contains the Ca II infrared

---

[1] Observations were made at the Palomar Observatory as part of a collaborative agreement between California Institute of Technology and the Carnegie Institution of Washington.

TABLE 1

OBSERVATIONAL MATERIAL

Galaxy	Type *M*	Axis	Date	Slit	Wavelength Region	Camera	Exposure (s)	Seeing
NGC 2841.........	Sb	major	1981 Mar 9	1″	Mg I *b*	blue	1800	2″
	−21.5	minor	1981 Mar 9	1	Mg I *b*	blue	1800	2
NGC 3898.........	Sa	minor	1981 Mar 9	1	Mg I *b*	blue	1800	2
	−21.04	major	1981 Mar 9	1	Mg I *b*	blue	1800	2
		major	1981 Mar 10	2	Hα	blue	9000	2
NGC 4450.........	Sab	major	1981 Apr 27	2	Hα	blue	7200	3.5
	−21.4	major	1981 Apr 27	1	Mg I *b*	blue	3300	3.5
NGC 4569.........	Sab	major	1981 Mar 9	1	Mg I *b*	blue	1800	2
	−22.31	major	1981 Mar 10	2	Hα	blue	10000	2
		major	1982 Apr 28	2	Ca triplet	red	9000	1.5
		major	1983 Apr 5	1	Hα	red	1500	1.5
NGC 5055.........	Sbc	major	1982 Apr 29	2	Hα	blue	9000	4
	−21.34	minor	1982 Apr 29	2	Ca triplet	red	2500	4
		major	1982 Apr 29	2	Ca triplet	red	9000	4
NGC 5879.........	Sb	major	1982 Apr 28	2	Hα	blue	8000	1.5
	−20.4	major	1982 Apr 28	2	Ca triplet	red	8000	1.5

NOTES.—The type and absolute visual magnitude are taken from Sandage and Tammann 1981. Observations of Hα region are emission-line measurements. Observations of Mg I *b* or Ca triplet region are absorption-line measurements. Blue camera has 0″.78 per pixel. Red camera has 0″.58 per pixel.

triplet. The calcium triplet and Hα regions were often observed simultaneously by replacing the normal dichroic, which splits the light between the two optical paths at 5200 Å, with one which splits the light at 6900 Å.

Details of the observations are listed in Table 1. A 2″ wide slit was used for most of the exposures. One pixel corresponds to 0″.78 on the blue side and 0″.58 on the red side. The slit was ~120″ long, and for most of the emission-line (the Hα region) observations, the nucleus of the galaxy was placed near one end. For the Mg I *b* exposures, the nucleus was centered along the slit. Comparison lamp exposures were taken after every object integration, and late G or early K giants were observed for templates with the same setup on each night that we obtained absorption-line data. All observations were made with gratings having 1200 grooves mm^{-1} used in first order. These gratings give a reciprocal dispersion of ~1 Å per pixel, and the resolution was about 2.6 Å for both the blue and red cameras with a 2″ slit.

The frames were all bias subtracted and flat-field corrected. The two-dimensional spectra were then separated into groups of one-dimensional spectra, composed of individual rows in regions where the signal was strong and averages of several rows in other regions. For each object spectrum, the same rows of the accompanying comparison frame were averaged and the resulting comparison line positions were used to determine a wavelength polynomial. This procedure removes the effects of distortion in the spectrograph and any slight tilt of the slit with respect to the CCD pixel columns. The wavelength functions were cubic polynomials fitted to between 8 and 15 arc lines. The residuals in the fits were typically 0.05 Å or less. This corresponds to ~4 km s^{-1} uncertainty due to the wavelength calibration. Moreover, the residuals of a given comparison line were similar from fit to fit, suggesting that the relative velocities along the slit are measurable to even higher accuracy than this.

The emission-line spectra were measured by fitting a Gaussian to each of the five emission lines in the wavelength region observed. The center of the Gaussian was converted to a velocity, and a heliocentric correction was applied. The velocities were then averaged with approximate weighting by the strengths of the individual lines.

The resulting rotation curves are presented in Table 2. The position angles listed for each observation give the direction of the positive axis. Note that in some cases the velocities are determined from the sum of a number of rows. These velocities are listed only for the central row in such a sum. In practice, the shorter exposures were of insufficient quality to yield precise information. Thus, we were unable to use any of the minor-axis emission-line frames or the major-axis emission-line frame for NGC 2841. By summing the pixel counts between the major emission lines, a rough continuum intensity (hereafter CI) measurement can be made; these are also listed in Table 2. Because the galaxies in this sample have large angular extent, the slit did not reach sufficiently far for a reliable measurement of the sky brightness. Thus, accurate sky subtraction was not possible, so the CI values may have systematic errors.

In addition to the velocities, the reduction procedure yielded line widths for the emission lines in each spectrum. These values are not presented here, but we describe the general trends seen. In all objects, the lines were unresolved ($\sigma < 40$ km s^{-1}) at radii greater than ~5″. Within this radius, they broadened, reaching widths (Gaussian standard deviations) of 100–150 km s^{-1} at the centers. Some fraction of these widths comes from the rotation of the material and is dependent upon slit width and seeing.

The absorption-line frames were reduced using the Fourier quotient method developed by Schechter (Sargent *et al.* 1977). The sky was determined either from the edges of each object frame or from separate sky frames and was subtracted from the object frames. Tilts in the slit relative to the detector were removed for galaxy and template star frames. The rows of each frame were co-added such that the signal-to-noise ratio in a one-dimensional spectrum was at least 30. The choice to limit ourselves to such high signal-to-noise ratio spectra was made because of potential systematic errors in low light level exposures on CCDs. Problems at low light levels may arise because of poor charge transfer efficiency. The combination of this limit

TABLE 2

EMISSION-LINE ROTATION CURVES

Galactocentric Distance (arcsecs)	Continuum Intensity	Radial Velocity (km/sec)	Galactocentric Distance (arcsecs)	Continuum Intensity	Radial Velocity (km/sec)
NGC 3898 Major Axis - PA = 287					
-75.66	-15		-30.42	74	
-74.88	-6		-29.64	74	
-74.10	1		-28.86	98	
-73.32	2		-28.08	91	
-72.54	6		-27.30	89	
-71.76	4	1380	-26.52	91	
-70.98	7		-25.74	91	
-70.20	10		-24.96	95	
-69.42	18		-24.18	104	
-68.64	14		-23.40	116	
-67.86	14		-22.62	125	
-67.08	13		-21.84	125	
-66.30	15		-21.06	132	
-65.52	16		-20.28	146	
-64.74	-3		-19.50	154	
-63.96	41		-18.72	161	1372
-63.18	19		-17.94	176	
-62.40	14		-17.16	197	
-61.62	16		-16.38	207	
-60.84	21		-15.60	223	
-60.06	17		-14.82	249	1430
-59.28	15		-14.04	274	
-58.50	16		-13.26	300	
-57.72	17		-12.48	328	
-56.94	20		-11.70	356	
-56.16	22		-10.92	388	1401
-55.38	28		-10.14	423	
-54.60	33		-9.36	458	
-53.82	32		-8.58	509	
-53.04	23	1342	-7.80	563	
-52.26	53		-7.02	634	1357
-51.48	38		-6.24	748	
-50.70	37		-5.46	901	
-49.92	37		-4.68	1069	1325
-49.14	42		-3.90	1355	1308
-48.36	40		-3.12	1810	1287
-47.58	39		-2.34	2579	1238
-46.80	44		-1.56	3885	1215
-46.02	40		-0.78	5588	1193
-45.24	45		0.00	6582	1185
-44.46	41		0.78	5781	1174
-43.68	39		1.56	4267	1169
-42.90	41		2.34	2925	1157
-42.12	47		3.12	2078	1135
-41.34	40		3.90	1571	1108
-40.56	60		4.68	1240	1082
-39.78	51		5.46	1025	1042
-39.00	46		6.24	870	1039
-38.22	47		7.02	754	1028
-37.44	45		7.80	671	1034
-36.66	54		8.58	610	1042
-35.88	55		9.36	558	1014
-35.10	54		10.14	499	1022
-34.32	57		10.92	453	
-33.54	56		11.70	424	
-32.76	60		12.48	382	
-31.98	66		13.26	347	
-31.20	66		14.04	327	
NGC 4450 Major Axis - PA = 183					
-78.78	42		-27.30	114	2043
-78.00	24		-26.52	113	
-77.22	35		-25.74	115	
-76.44	39		-24.96	117	2049
-75.66	16		-24.18	121	

TABLE 2—*Continued*

Galactocentric Distance (arcsecs)	Continuum Intensity	Radial Velocity (km/sec)	Galactocentric Distance (arcsecs)	Continuum Intensity	Radial Velocity (km/sec)
-74.88	18		-23.40	122	
-74.10	16		-22.62	123	2047
-73.32	16		-21.84	133	
-72.54	19		-21.06	141	
-71.76	13		-20.28	153	
-70.98	7		-19.50	156	
-70.20	13		-18.72	159	
-69.42	17		-17.94	170	2048
-68.64	19		-17.16	177	
-67.86	18		-16.38	174	
-67.08	18		-15.60	183	
-66.30	18		-14.82	202	2054
-65.52	20		-14.04	220	
-64.74	16		-13.26	234	
-63.96	12		-12.48	251	2064
-63.18	25		-11.70	272	
-62.40	17		-10.92	287	
-61.62	22		-10.14	314	2082
-60.84	20		-9.36	336	
-60.06	20		-8.58	367	2101
-59.28	23		-7.80	398	2109
-58.50	23	2068	-7.02	452	2102
-57.72	21		-6.24	510	2108
-56.94	18		-5.46	576	2112
-56.16	23		-4.68	668	2100
-55.38	25		-3.90	800	2086
-54.60	26		-3.12	995	2076
-53.82	30	2024	-2.34	1282	2028
-53.04	32		-1.56	1768	2005
-52.26	43		-0.78	2593	2024
-51.48	48		0.00	3449	1972
-50.70	44		0.78	3423	1975
-49.92	50		1.56	2621	1980
-49.14	50		2.34	1884	1974
-48.36	53	2024	3.12	1436	1970
-47.58	55		3.90	1141	1935
-46.80	62		4.68	928	1928
-46.02	63		5.46	765	1937
-45.24	68		6.24	635	1936
-44.46	72		7.02	543	1935
-43.68	76		7.80	480	1932
-42.90	77	2028	8.58	427	1924
-42.12	81		9.36	388	1922
-41.34	80		10.14	357	1940
-40.56	92		10.92	333	1939
-39.78	93		11.70	310	
-39.00	91		12.48	279	1940
-38.22	93		13.26	254	
-37.44	100	2041	14.04	241	
-36.66	103		14.82	217	1963
-35.88	99		15.60	188	
-35.10	99		16.38	165	
-34.32	105		17.16	141	
-33.54	109	2040	17.94	123	
-32.76	111		18.72	108	
-31.98	110	2047	19.50	105	
-31.20	109		20.28	98	
-30.42	109		21.06	101	
-29.64	110	2042	21.84	98	
-28.86	115		22.62	103	
-28.08	117		23.40	102	
NGC 4569 Major Axis 3/10/81 - PA = 203					
-79.56	54		-28.08	226	
-78.78	54		-27.30	232	
-78.00	68		-26.52	237	
-77.22	55		-25.74	243	-102
-76.44	44		-24.96	245	

TABLE 2—*Continued*

Galactocentric Distance (arcsecs)	Continuum Intensity	Radial Velocity (km/sec)	Galactocentric Distance (arcsecs)	Continuum Intensity	Radial Velocity (km/sec)
-75.66	40		-24.18	260	
-74.88	40		-23.40	261	
-74.10	37		-22.62	273	
-73.32	57		-21.84	271	-125
-72.54	53		-21.06	280	
-71.76	57		-20.28	297	
-70.98	54		-19.50	308	
-70.20	48		-18.72	315	
-69.42	47		-17.94	325	-117
-68.64	66	-58	-17.16	334	
-67.86	69	-59	-16.38	354	
-67.08	78	-63	-15.60	374	
-66.30	82	-69	-14.82	381	
-65.52	88	-70	-14.04	399	-148
-64.74	92	-71	-13.26	411	
-63.96	95	-71	-12.48	428	
-63.18	101	-69	-11.70	445	
-62.40	111	-71	-10.92	462	
-61.62	118	-70	-10.14	499	-156
-60.84	125	-67	-9.36	540	
-60.06	129		-8.58	577	
-59.28	117		-7.80	606	
-58.50	110	-74	-7.02	667	-165
-57.72	124	-65	-6.24	787	-170
-56.94	137	-61	-5.46	993	-174
-56.16	134	-54	-4.68	1350	-193
-55.38	138	-54	-3.90	1904	-208
-54.60	141	-53	-3.12	2820	-225
-53.82	142	-42	-2.34	4386	-250
-53.04	149	-55	-1.56	7260	-249
-52.26	155	-78	-0.78	1493	-247
-51.48	149	-78	0.00	5586	-247
-50.70	155	-79	0.78	3199	-245
-49.92	142	-71	1.56	7039	-232
-49.14	141	-74	2.34	3760	-238
-48.36	138	-74	3.12	2249	-246
-47.58	146	-80	3.90	1420	-249
-46.80	142	-82	4.68	972	-249
-46.02	143	-80	5.46	747	-253
-45.24	144	-81	6.24	643	-252
-44.46	148	-86	7.02	574	
-43.68	166	-81	7.80	526	
-42.90	190	-76	8.58	495	
-42.12	223	-71	9.36	468	
-41.34	254	-69	10.14	454	
-40.56	250	-67	10.92	437	
-39.78	244	-67	11.70	417	
-39.00	227	-74	12.48	408	
-38.22	209	-79	13.26	395	
-37.44	193	-82	14.04	389	
-36.66	192	-81	14.82	402	
-35.88	204	-75	15.60	433	
-35.10	212	-64	16.38	400	
-34.32	211	-59	17.16	347	
-33.54	209	-50	17.94	312	
-32.76	217	-75	18.72	298	
-31.98	215	-88	19.50	288	
-31.20	215	-83	20.28	282	
-30.42	212		21.06	274	
-29.64	215		21.84	276	
-28.86	217		22.62	283	
NGC 4569 Major Axis 4/05/83 - PA = 203					
-57.42	65	-67	0.00	1763	-252
-56.84	69	-58	0.58	1437	-265
-56.26	66	-58	1.16	920	-256
-55.68	44	-65	1.74	575	-245
-55.10	32	-66	2.32	375	-261

1986ApJ...302..208F

TABLE 2—*Continued*

Galactocentric Distance (arcsecs)	Continuum Intensity	Radial Velocity (km/sec)	Galactocentric Distance (arcsecs)	Continuum Intensity	Radial Velocity (km/sec)
-54.52	26	-63	2.90	257	-259
-53.94	22	-63	3.48	177	-267
-53.36	13		4.06	122	-274
-52.78	16	-70	4.64	92	-281
-52.20	3		5.22	-9	-287
-51.62	18		5.80	81	
-51.04	12	-74	6.38	62	-282
-50.46	10		6.96	65	
-49.88	14		7.54	56	
-49.30	8	-78	8.12	54	-285
-48.72	7		8.70	53	
-48.14	2		9.28	53	
-47.56	4	-81	9.86	48	-302
-46.98	3		10.44	49	
-46.40	1		11.02	45	
-45.82	2	-94	11.60	40	-297
-45.24	5		12.18	44	
-44.66	6		12.76	48	
-44.08	11	-91	13.34	44	-299
-43.50	9		13.92	41	
-42.92	10		14.50	49	
-42.34	6	-94	15.08	53	
-41.76	13		15.66	51	
-41.18	12		16.24	41	
-40.60	16	-96	16.82	36	
-40.02	16		17.40	38	
-39.44	19		17.98	32	
-38.86	18	-97	18.56	36	
-38.28	16		19.14	29	
-37.70	18		19.72	31	
-37.12	19	-93	20.30	32	
-36.54	22		20.88	32	
-35.96	17		21.46	26	
-35.38	14	-95	22.04	30	
-34.80	17		22.62	29	
-34.22	24		23.20	29	
-33.64	18	-98	23.78	25	
-33.06	22		24.36	22	
-32.48	12		24.94	29	
-31.90	18		25.52	26	
-31.32	20		26.10	23	
-30.74	22	-102	26.68	26	
-30.16	26		27.26	24	
-29.58	22		27.84	25	
-29.00	24		28.42	24	
-28.42	2		29.00	24	
-27.84	32		29.58	25	
-27.26	31		30.16	24	
-26.68	29	-102	30.74	28	
-26.10	27		31.32	21	
-25.52	29		31.90	7	
-24.94	32		32.48	29	
-24.36	25		33.06	25	
-23.78	28		33.64	32	
-23.20	29		34.22	25	
-22.62	29	-113	34.80	29	
-22.04	24		35.38	19	
-21.46	35		35.96	30	
-20.88	36		36.54	29	
-20.30	30		37.12	25	
-19.72	36		37.70	20	
-19.14	32		38.28	23	
-18.56	31	-107	38.86	24	
-17.98	38		39.44	15	
-17.40	32		40.02	15	

TABLE 2—*Continued*

Galactocentric Distance (arcsecs)	Continuum Intensity	Radial Velocity (km/sec)	Galactocentric Distance (arcsecs)	Continuum Intensity	Radial Velocity (km/sec)
-16.82	40		40.60	17	
-16.24	39		41.18	23	
-15.66	43		41.76	15	
-15.08	42		42.34	15	
-14.50	45	-195	42.92	10	
-13.92	42		43.50	11	
-13.34	43		44.08	-33	
-12.76	42		44.66	7	
-12.18	47		45.24	11	
-11.60	43		45.82	5	
-11.02	47		46.40	8	
-10.44	53		46.98	8	
-9.86	52		47.56	0	
-9.28	60		48.14	14	
-8.70	56		48.72	7	
-8.12	62		49.30	11	
-7.54	68		49.88	8	
-6.96	75		50.46	4	
-6.38	85		51.04	-8	
-5.80	100		51.62	14	
-5.22	123		52.20	13	
-4.64	159		52.78	9	
-4.06	209		53.36	11	
-3.48	267		53.94	2	
-2.90	342		54.52	5	
-2.32	92		55.10	6	
-1.74	626	-246	55.68	-4	
-1.16	1055	-248	56.26	5	
-0.58	1548	-248			
		NGC 5055 Major Axis - PA = 105			
-30.42	-49		24.18	119	646
-29.64	176	347	24.96	117	
-28.86	118	340	25.74	113	
-28.08	118	345	26.52	106	652
-27.30	126	343	27.30	106	
-26.52	135	356	28.08	101	
-25.74	143		28.86	106	658
-24.96	146	336	29.64	107	
-24.18	156		30.42	107	
-23.40	158		31.20	92	657
-22.62	161	338	31.98	95	
-21.84	161	341	32.76	101	
-21.06	155	345	33.54	108	662
-20.28	158	343	34.32	112	
-19.50	171	346	35.10	116	
-18.72	173	355	35.88	118	656
-17.94	180	351	36.66	118	
-17.16	173	354	37.44	106	
-16.38	182	360	38.22	96	640
-15.60	190	371	39.00	94	
-14.82	191	371	39.78	87	
-14.04	197		40.56	84	656
-13.26	208		41.34	86	
-12.48	220	389	42.12	87	
-11.70	231		42.90	87	654
-10.92	238		43.68	82	
-10.14	251	393	44.46	87	
-9.36	255		45.24	83	650
-8.58	264		46.02	86	
-7.80	259	403	46.80	76	
-7.02	287		47.58	77	666
-6.24	327		48.36	84	
-5.46	387	403	49.14	84	
-4.68	457		49.92	82	658
-3.90	567	419	50.70	73	

TABLE 2—*Continued*

Galactocentric Distance (arcsecs)	Continuum Intensity	Radial Velocity (km/sec)	Galactocentric Distance (arcsecs)	Continuum Intensity	Radial Velocity (km/sec)
-3.12	782	414	51.48	66	
-2.34	1219	455	52.26	63	651
-1.56	1929	478	53.04	62	
-0.78	2449	499	53.82	56	
0.00	2589	519	54.60	53	663
0.78	2307	546	55.38	54	
1.56	1461	576	56.16	53	
2.34	930	584	56.94	52	664
3.12	695	597	57.72	51	
3.90	542	609	58.50	51	
4.68	459	604	59.28	53	667
5.46	397	623	60.06	52	
6.24	351	630	60.84	53	
7.02	325	630	61.62	51	684
7.80	289	636	62.40	51	
8.58	273	627	63.18	51	
9.36	247	654	63.96	47	671
10.14	225		64.74	48	
10.92	210		65.52	47	
11.70	197		66.30	47	665
12.48	143	647	67.08	50	
13.26	146		67.86	50	
14.04	142		68.64	48	663
14.82	124	624	69.42	47	
15.60	126		70.20	49	
16.38	113		70.98	49	
17.16	114	653	71.76	49	
17.94	120		72.54	57	660
18.72	123		73.32	72	
19.50	125	630	74.10	83	
20.28	128		74.88	106	
21.06	130		75.66	125	
21.84	126	640	76.44	138	
22.62	129		77.22	147	666
23.40	123				
NGC 5879 Major Axis = PA 174					
-26.52	3		24.96	35	638
-25.74	4	932	25.74	31	620
-24.96	1		26.52	32	636
-24.18	4		27.30	31	656
-23.40	5	933	28.08	30	659
-22.62	14		28.86	31	668
-21.84	20	905	29.64	27	
-21.06	25	893	30.42	25	672
-20.28	33	892	31.20	22	
-19.50	37	892	31.98	22	
-18.72	43	886	32.76	21	669
-17.94	48	892	33.54	21	
-17.16	49	893	34.32	20	
-16.38	53	895	35.10	16	673
-15.60	54	885	35.88	16	
-14.82	58	881	36.66	16	
-14.04	58	883	37.44	17	678
-13.26	59	887	38.22	17	
-12.48	67	884	39.00	19	
-11.70	70	881	39.78	17	660
-10.92	77	885	40.56	16	
-10.14	85	873	41.34	19	
-9.36	88	869	42.12	15	662
-8.58	89	874	42.90	14	
-7.80	94	865	43.68	14	
-7.02	97	858	44.46	12	659
-6.24	100	837	45.24	15	
-5.46	108	831	46.02	13	
-4.68	111	828	46.80	13	650
-3.90	121	829	47.58	14	

TABLE 2—*Continued*

Galactocentric Distance (arcsecs)	Continuum Intensity	Radial Velocity (km/sec)	Galactocentric Distance (arcsecs)	Continuum Intensity	Radial Velocity (km/sec)
-3.12	136	827	48.36	13	
-2.34	171	806	49.14	16	
-1.56	212	791	49.92	13	
-0.78	251	772	50.70	13	
0.00	274	764	51.48	10	
0.78	248	758	52.26	11	
1.56	225	729	53.04	10	
2.34	195	739	53.82	8	
3.12	172	726	54.60	11	
3.90	146	717	55.38	9	
4.68	122	706	56.16	9	
5.46	108	698	56.94	7	
6.24	96	698	57.72	8	
7.02	88	704	58.50	7	
7.80	80	708	59.28	7	
8.58	80	699	60.06	7	
9.36	75	693	60.84	8	
10.14	73	691	61.62	10	
10.92	69	680	62.40	10	
11.70	65	672	63.18	13	
12.48	53	665	63.96	11	
13.26	35	656	64.74	11	
14.04	29	658	65.52	12	
14.82	29	654	66.30	12	
15.60	32	660	67.08	10	
16.38	32	657	67.86	10	
17.16	32	656	68.64	11	
17.94	34	651	69.42	10	
18.72	37	638	70.20	11	
19.50	36	658	70.98	12	
20.28	39	652	71.76	12	
21.06	36	652	72.54	12	
21.84	37	658	73.32	13	
22.62	36	649	74.10	15	
23.40	34	646	74.88	17	
24.18	33	655	75.66	22	

and the readout noise of the chips has limited the radii to which we could accurately measure velocities to relatively small values compared with observations made with different kinds of detectors. Then each one-dimensional spectrum was wavelength calibrated and run through the Fourier quotient program, which outputs a velocity, a velocity dispersion, and an average line-strength factor.

The center of each galaxy was determined by finding the point around which the rotation curve is most symmetric, and the radial velocity at this point was considered the systemic velocity. This value was then subtracted from each other point, so all the rotation curves are centered on zero. Table 3 gives the absorption-line data, the rotation curves, and dispersion profiles used for each object in the sample.

III. MODELS

Our galaxy models contain two components: a bulge and a disk, each described below. Here we describe the coordinate systems used in the models. The models are axisymmetric, so we use a cylindrical-polar system (R, z, ϕ) of spatial coordinates in the galaxy. In the bulge, where an oblate spheroid is assured, ξ is a spheroidal coordinate which is constant along equidensity surfaces:

$$\xi^2 = R^2 + f^2 z^2 , \tag{1}$$

where f is the flattening parameter, related to the ellipticity ϵ by $f = (1 - \epsilon)^{-1}$. In the plane of the sky, a Cartesian system (p, q) aligned with the projected principle axes is used. The variable s is distance along the line of sight, where $s = 0$ is the plane passing through the galaxy center. The inclination of the galaxy is i; for edge-on $i = 0$. The two sets of coordinates are related by

$$R^2 = p^2 + (s \cos i - q \sin i)^2 , \tag{2}$$

$$z = s \sin i + q \cos i , \tag{3}$$

$$\xi^2 = \xi_0 + s\xi_1 + s^2 \xi_2 , \tag{4}$$

where

$$\begin{aligned} \xi_0 &= p^2 + q^2(\sin^2 i + f^2 \cos^2 i) , \\ \xi_1 &= 2q \sin i \cos i (f^2 - 1) , \\ \xi_2 &= f^2 \sin^2 i + \cos^2 i . \end{aligned} \tag{5}$$

For an observation point (p, q), minimum ξ occurs at

$$\xi_m^2 = \xi_0 - \frac{\xi_1^2}{4\xi_2} = p^2 + \frac{q^2}{s^2 + c^2 f^{-2}} . \tag{6}$$

TABLE 3

ABSORPTION-LINE VELOCITY DATA

Galactocentric Distance (arcsecs)	Mean Velocity (km/sec)	Velocity Dispersion (km/sec)	Galactocentric Distance (arcsecs)	Mean Velocity (km/sec)	Velocity Dispersion (km/sec)
			NGC 2841 Major Axis		
12.15	101	194	-0.72	-28	244
7.86	81	218	-1.50	-59	223
5.96	103	221	-2.28	-74	236
4.74	103	204	-3.06	-91	211
3.96	115	237	-3.84	-99	224
3.18	89	229	-4.62	-116	221
2.40	84	221	-5.40	-89	232
1.62	69	245	-6.57	-97	235
0.84	32	248	-8.52	-92	197
0.06	2	240	-12.03	-127	213
			NGC 2841 Minor Axis		
7.41	-18	226	-0.78	43	247
5.07	15	300	-1.56	45	252
3.90	16	270	-2.34	37	246
3.12	25	272	-3.12	-12	209
2.34	3	220	-3.90	97	230
1.56	12	230	-4.68	10	264
0.78	16	257	-5.85	15	230
0.00	29	241	-7.80	33	249
			NGC 3898 Major Axis		
6.68	64	104	-1.12	-36	202
3.95	49	146	-1.90	-53	211
2.78	56	163	-2.68	-48	186
2.00	66	192	-3.46	-58	162
1.22	34	207	-4.24	-95	228
0.44	14	220	-5.41	-87	182
-0.34	-7	215	-7.75	-86	155
			NGC 3898 Minor Axis		
3.51	-106	185	-1.56	-48	217
2.34	-70	208	-2.34	-50	217
1.56	-61	243	-3.12	-65	226
0.78	-64	239	-3.90	-15	319
0.00	-62	248	-5.07	-64	173
-0.78	-55	247			
			NGC 4450 Major Axis		
11.47	11	147	-0.62	-12	142
7.96	24	123	-1.40	-17	147
6.01	31	152	-2.18	-42	148
4.84	45	138	-2.96	-54	147
4.06	43	136	-3.74	-51	157
3.28	53	125	-4.52	-49	150
2.50	45	132	-5.69	-36	142
1.72	33	140	-7.64	-71	74
0.94	16	139	-10.76	-79	177
0.16	-3	139			
			NGC 4569 Major Axis 3/09/81		
3.12	70	110	-0.78	-38	155
2.34	56	148	-1.56	-59	138
1.56	59	145	-2.34	-88	108
0.78	35	154	-3.12	-86	102
0.00	0	157	-4.29	-107	109

TABLE 3—*Continued*

Galactocentric Distance (arcsecs)	Mean Velocity (km/sec)	Velocity Dispersion (km/sec)	Galactocentric Distance (arcsecs)	Mean Velocity (km/sec)	Velocity Dispersion (km/sec)
NGC 4569 Major Axis 4/28/82					
-10.15	-31	93	0.58	26	135
-8.12	-42	114	1.16	46	135
-6.67	-48	125	1.74	68	121
-5.51	-54	125	2.32	84	110
-4.64	-84	116	2.90	92	100
-4.06	-88	114	3.48	99	98
-3.48	-101	109	4.06	99	95
-2.90	-105	100	4.64	86	103
-2.32	-92	111	5.22	84	103
-1.74	-78	115	6.09	76	97
-1.16	-51	126	7.25	72	99
-0.58	-23	136	8.70	54	87
0.00	0	136	10.73	52	82
NGC 5055 Major Axis					
20.59	49	134	-0.58	-6	116
18.27	59	102	-1.16	-16	113
15.95	26	122	-1.74	-27	114
12.47	41	115	-2.32	-43	106
11.31	50	112	-2.90	-68	104
10.15	53	111	-3.48	-57	100
8.99	50	116	-4.06	-64	103
8.12	56	97	-4.64	-65	102
7.54	50	108	-5.22	-64	99
6.96	50	100	-5.80	-67	94
6.38	45	109	-6.38	-69	88
5.80	50	98	-6.96	-77	98
5.22	53	98	-7.83	-72	90
4.64	49	102	-8.99	-88	94
4.06	50	101	-10.15	-85	87
3.48	45	104	-11.31	-96	97
2.90	43	95	-12.47	-98	90
2.32	36	106	-13.63	-103	92
1.74	23	110	-14.79	-99	82
1.16	17	116	-15.95	-104	66
0.58	7	111	-17.11	-104	65
0.00	0	118	-18.56	-119	87
NGC 5055 Minor Axis					
5.51	-7	119	-0.58	-4	120
3.19	3	117	-1.16	6	113
2.32	4	117	-1.74	-8	110
1.74	3	114	-2.61	3	119
1.16	2	120	-4.06	2	120
0.58	4	117	-6.38	-11	114
0.00	3	120	-10.73	-3	111
NGC 5879 Major Axis					
-15.66	-111	38	0.58	11	72
-12.47	-106	40	1.16	20	73
-10.44	-98	51	1.74	9	83
-8.70	-84	48	2.32	26	78
-6.96	-75	54	2.90	37	72
-5.51	-56	57	3.77	38	74
-4.35	-42	61	4.93	49	62
-3.19	-36	65	6.09	74	33
-2.32	-29	68	7.25	68	63
-1.74	-20	78	8.70	83	53
-1.16	-19	79	10.44	95	60
-0.58	-9	73	12.18	99	63
0.00	0	71	14.21	105	59

a) Disk

We use the disk model from van der Kruit and Searle (1981*a*, 1982), which is an exponential disk with constant scale height. The density is specified by

$$\rho_D(R, z) = \rho_0 e^{-R/R_D} \operatorname{sech}^2 (z/z_0) , \tag{7}$$

where ρ_0 is the central density, R_D is the disk scale length, and z_0 is twice the scale height. These authors have shown this model to be a reasonable representation of the disk surface brightness out to a few scale lengths, after which it rapidly drops off (see also Seiden, Schulman, and Elmegreen 1984). We do not impose an outer edge in our models because the range of our observations is interior to the typically observed cutoff radius. This exclusion might cause a slight systemic overestimate in our disk masses. The surface density is calculated by integrating equation (7) over z:

$$\mu_D(R) = \mu_0 e^{-R/R_D} , \tag{8}$$

where the central surface density $\mu_0 = 2\rho_0 z_0$. The total mass M_D is $2\pi\mu_0 R_D^2$. Note that the disk surface density can be determined by R_D and M_D without specifying the scale height. The light and the acceleration from the disk are calculated assuming the disk is very thin and has a constant mass-to-light ratio M_D/L_D. The scale height is used only to compute the velocity dispersion, which we assume to be isotropic (see Bahcall 1984),

$$\sigma_D^2(R) = \pi G \mu_D(R) z_0 . \tag{9}$$

Since the disk is thin and the galaxies in this sample are not edge-on, line-of-sight projection effects will be ignored for the disk component.

b) Bulge

The bulge component is modeled as an oblate spheroid whose flattening is specified by its true ellipticity $\epsilon = 1 - b/a$, where b/a is the axial ratio. The bulge ellipticity is assumed to be constant even though observations of other galaxies show an outward increase in the flattening (van der Kruit and Searle 1981*a*, 1981*b*, 1982). This effect is probably caused by the presence of the disk, but to include it is beyond the scope of this paper.

Observations of many disk systems (Kormendy 1977; Burstein 1979; Boroson 1981) have shown that the bulge surface brightness is acceptably represented by a de Vaucouleurs' law (1948), which in magnitudes is

$$\mu^m(p) = \mu_e^m + 8.325[(p/R_e)^{1/4} - 1] , \tag{10}$$

where R_e is the effective radius and μ_e^m is the surface brightness at R_e, measured along the major axis. The bulge density profiles are fits to a deprojected $r^{1/4}$ law taken from approximate formulae derived by Young (1976) and Tonry (1984*b*). The density on a spheroidal surface is

$$\rho_B(\xi) = f M_B R_e^{-3} \rho^*(\xi/R_e) , \tag{11}$$

where $f\rho^*$ is a dimensionless function whose total volume integral is unity and M_B is the total bulge mass.

Along with the mass model we must know the three-dimensional velocity structure of the bulge. This information cannot be entirely obtained from observations, so we must make some assumptions. We use the mean rotation velocity in the equatorial plane as an independent function to be determined by fitting the observations, but we assume the mean rotation out of the plane follows the scaling

$$u(R, z) \approx \frac{u_0(R)}{[1 + (z/R)^2]^{1/2}} , \tag{12}$$

where u_0 is the mean rotation in the equatorial plane. This scaling was derived by using $\rho^* \propto \xi^{-2}$ and computing the circular velocity for an oblate spheroid at low z and to first order in ϵ; this result is sufficiently accurate for $\epsilon \leq 0.4$. We then assume that the mean rotation rate scales in the same way as the circular velocity. Note that adopting this relation is equivalent to assuming that the angular velocity is constant on spheroidal shells, in which case u_0 is a function of ξ, not R. If the equatorial rotation curve is flat, these two forms give the same result.

The relation (12) has been tested on measurements of edge-on disk galaxies; projection effects have been ignored. Kormendy and Illingworth (1982, hereafter KI), measured v and σ along slits both parallel and perpendicular to the major axis. Two of their four galaxies fitted the above relation quite well, as shown in Figure 1; these are bulge-dominated systems with dynamically significant rotation. The other two galaxies do not fit the relation; for these there is a large difference in the bulge and disk rotation rates so a fit cannot be found.

We must also assume the form of the velocity dispersion structure. We shall use the radial velocity dispersion in the equatorial plane as an independent function $\sigma_R(R)$. We allow for anisotropy in our models, but as will be shown, it is not necessary to invoke it. Since the projected velocity dispersion in KI's galaxies did not change significantly with z, we shall assume that σ_R and σ_ϕ are not a function of z. This assumption is imposed only to simplify the model. If σ_R decreases outward, this predicts that the line-of-sight velocity dispersion, σ_s, observed along the minor axis falls off more slowly than along the major axis, since over-the-pole line of sight pulls the mean value up. This is in agreement with our minor axis data.

A pressure-supported, isotropic spheroid whose density distribution follows a deprojected de Vaucouleurs's law has central depression in the velocity dispersion (Binney 1980). The projected velocity dispersion peaks near $\sim 0.1 R_e$. Two plausible modifications can remove this depression; first, the addition of a central point mass, which causes the surrounding stars to move faster. Only 15% additional mass inside $\sim 0.1 R_e$ is sufficient to keep σ_s rising inward. Alternatively, a core radius may be introduced into the density profile, which decreases the number of slow-moving stars near the center, so the (mass-weighted) velocity dispersion increases. This deviation from de Vaucouleurs's law should be visible in high-resolution surface brightness measurements unless the mass-to-light ratio decreases in the center. Previous surface brightness studies of ellipticals reveal that some show a central core radius, while others follow a $r^{1/4}$ law to the seeing limit (Schweizer 1979). However, most bulges are smaller than those ellipticals, so seeing effects severely limit the detectability of cores.

c) Projection and Measurement Effects

External galaxies are, of course, seen only in the plane of the sky, so we must calculate how these models would appear in projection in order to compare them with observations. Here we discuss the projection of the bulge component; subsequently we will detail the procedure for including the disk. The

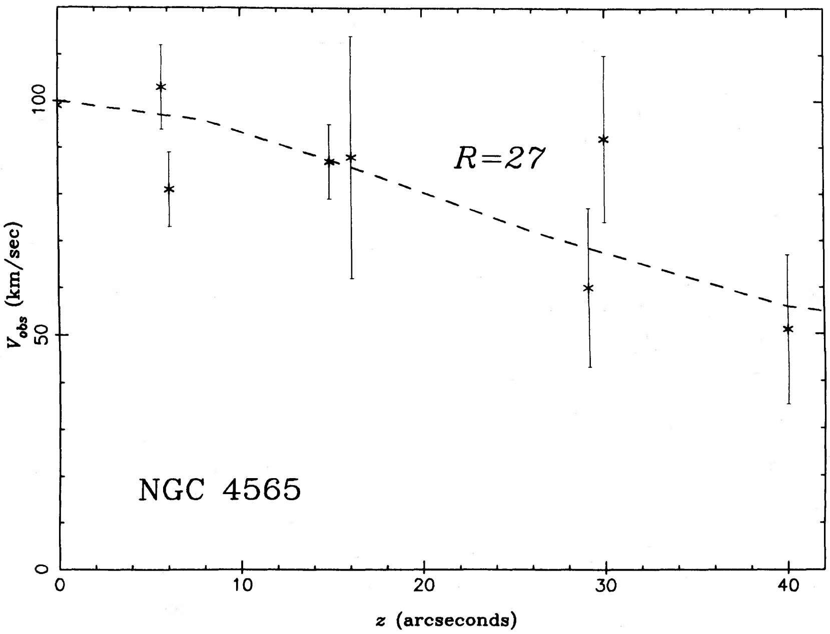

FIG. 1*a*

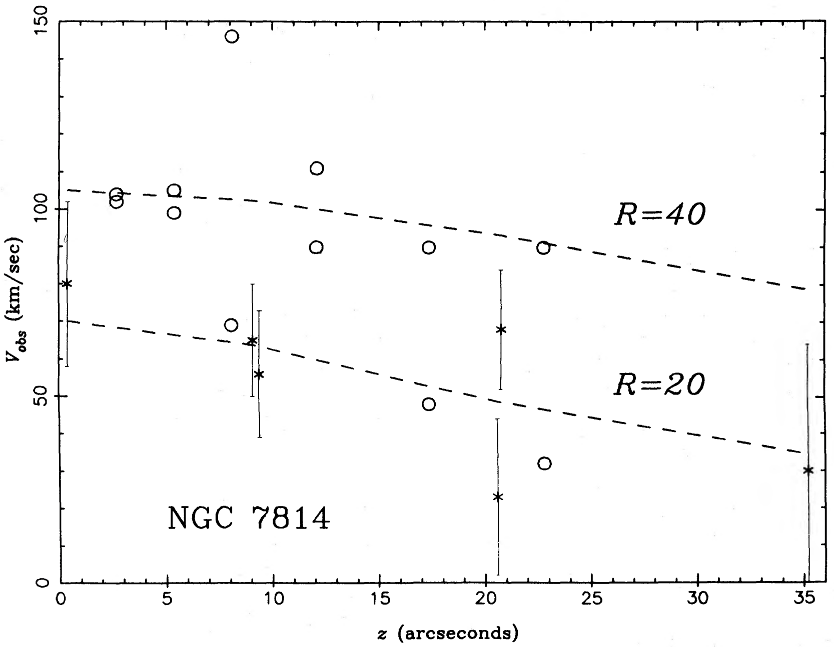

FIG. 1*b*

FIG. 1.—(*a*) Comparison of KI data for NGC 4565 to spheroidal rotation. Symbols are the rotation rate measured with the slit perpendicular to major axis at a distance R from the center. Dashed lines are model values from eq. (12). (*b*) Same as (*a*) for NGC 7814. Error bars are not included for $R = 40''$ points to avoid confusion.

bulge model is specified by ϵ, R_e, M_B, M_B/L_B, and the three-dimensional kinematic assumptions. First, we will calculate line-of-sight quantities; a subscript s will be used on some variables to denote integration along s.

The surface brightness is

$$\mu_L(p, q) = \int_{-\infty}^{\infty} \rho_L(\xi) ds , \qquad (13)$$

where ρ_L is the luminosity density $\rho(\xi)L_B/M_B$. For the special case of an oblate spheroid,

$$\mu_L(p, q) = \frac{2\xi_m}{\xi_2^{1/2}} \int_1^{\infty} \frac{\rho_L(\xi_m x) x dx}{(x^2 - 1)^{1/2}} . \qquad (14)$$

Because μ_L is a function only of $\xi_m(p, q)$ the isophotes are elliptical (see eq. [6]). The projected mean rotation is

$$v_s(p, q) = \mu_L^{-1} \int_{-\infty}^{\infty} \rho_L u(R, z) \frac{p \cos i}{R} ds . \qquad (15)$$

The observed velocity dispersion has several components; first, the true velocity dispersion must be projected:

$$\sigma_s^2(p, q) = \mu_L^{-1} \int_{-\infty}^{\infty} \rho_L \sigma_R^2 \left(1 - \beta \frac{p^2 \cos^2 i}{R^2} - \beta_z \sin^2 i\right) ds \,, \tag{16}$$

where β and β_z are anisotropy parameters, $\beta = 1 - \sigma_\phi^2/\sigma_R^2$, and $\beta_z = 1 - \sigma_z^2/\sigma_R^2$. Second, the contribution from the projection of the rotation curve is

$$\sigma_{vr}^2(p, q) = \langle u^2 \rangle_{\rm los} - v_s^2(p, q) \,, \tag{17}$$

where the mean-squared line-of-sight velocity is

$$\langle u^2 \rangle_{\rm los} = \mu_L^{-1} \int_{-\infty}^{\infty} \rho_L u^2 \frac{p^2 \cos^2 i}{R^2} ds \,. \tag{18}$$

These integrals can be performed analytically if idealizations such as a power-law luminosity density and flat rotation curves are assumed. In typical cases one finds $v_s/u \approx 60\%$–80% and $\sigma_{vr}/u \approx 20\%$–$30\%$ (see also Tonry 1984*a*; Young *et al.* 1978).

The observed quantities are modified by atmospheric seeing and instrumental resolution. We denote the broadening function as S; its integral is unity. Convolution will be denoted by an asterisk. The model " observed " surface brightness is

$$\mu_{\rm obs} = S * \mu_L \,. \tag{19}$$

Rotation curve and velocity dispersion profiles are modified by a luminosity-weighted convolution, defined as

$$P * f \equiv \frac{S * (\mu_L f)}{S * \mu_L} \,. \tag{20}$$

Thus,

$$v_{\rm obs}(p, q) = P * v_s \,. \tag{21}$$

The observed line width is increased because the mean velocity (line center) is simultaneously observed at many different projected spots on the galaxy by a finite-sized aperture (plus atmospheric agitation). The additional contribution to the observed velocity dispersion from an aperture is

$$\sigma_{\rm ap}^2 = P * v_s^2 - v_{\rm obs}^2 \,, \tag{22}$$

which is significant only near the center, if at all. The predicted total velocity dispersion is

$$\sigma_{\rm obs}^2 = P * (\sigma_s^2 + \langle u^2 \rangle_{\rm los}) - v_{\rm obs}^2 \,. \tag{23}$$

Since we have a two-component model, the true first and second moments of the line-of-sight velocity should be the sum of the two components weighted by their relative surface brightness. However, the measured moments do not directly represent the true moments because the observations were reduced using a Fourier quotient method (abbreviated FQ hereafter; see § II). This technique fits a Gaussian to the line-broadening profile, but the superposition of two components can be a distinctly non-Gaussian profile; this fitting error biases the measured values (Illingworth and Schechter 1982; Whitmore 1980; McElroy 1983; Whitmore, Rubin, and Ford 1984, hereafter WRF). In our situation the biases are competing; the method emphasizes the narrower component (disk) but is more sensitive to the stronger line component (bulge).

First, we must consider the bias effect on the measured mean velocity. If the fraction of bulge light contributed at a particular projected location is $b = \mu_b/\mu_{\rm tot}$ and the velocity difference between the two components is Δv, then the expected measured velocity $v_{\rm exp} = \Delta v(1 - b)$. However, the measured value v_m is frequently different from $v_{\rm exp}$, so we define an effective fraction from $v_m = \Delta v(1 - b_{\rm eff})$, so

$$1 - b_{\rm eff} \equiv \frac{v_m}{v_{\rm exp}} (1 - b) \,. \tag{24}$$

Thus, $b_{\rm eff}$ indicates what fraction of light the bulge would have to contribute to achieve the same measured value if the FQ method properly returned the mean velocity. Figure 2 shows

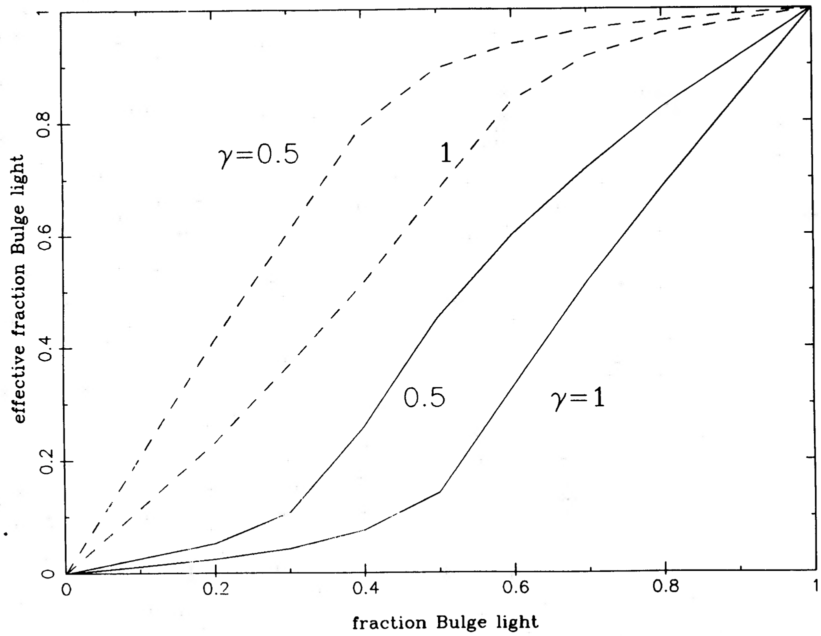

FIG. 2.—Effect of line strength and velocity dispersion on measurements via Fourier quotient method. The effective fraction of bulge light indicates what fraction of light the bulge would have to contribute to achieve the same measured velocity if the FQ method introduced no bias. Line strength γ of the bulge is 1 and the disk either 0.5 or 1, as labeled. Solid lines are for $\sigma_B/\sigma_D = 4./0.7$, dashed lines for $\sigma_B/\sigma_D = 0.7/2.5$.

the difference between mixing two components of equal line strength and mixing one component with half the line strength of the other. The result is that the absorption-line data mostly reflect the bulge rotation even in regions where the disk light contributes a significant fraction of the light (WRF).

The velocity dispersion expected from the combination of two components is not a simple linear interpolation between the two values. Fitting a Gaussian to two components with a nonzero separation in the mean values can result in a much larger width than either component. The expected value is

$$\sigma_{\rm exp}^2 = b\sigma_B^2 + (1 - b)\sigma_D^2 + b(1 - b)(\Delta v)^2 \, , \tag{25}$$

where Δv is the mean separation between the components. The measured values from the FQ method will not follow this relation because it is biased toward the narrower component; in worst cases, $\sigma_{\rm meas}$ will be 30% below $\sigma_{\rm exp}$.

Different authors have used different schemes to compute the goodness of fit of a Gaussian to the Fourier quotient (e.g., Sargent *et al.* 1977; Dressler 1979). The goal is to choose the best fit, despite noise in the data, particularly at high wavenumbers. Our tests show that biases introduced by typical goodness-of-fit tests are smaller than those inherent in the method when two components are present.

d) Fitting Procedure

In this section we detail the procedure used to fit a kinematic model to velocity data while satisfying physical constraints.

Two of the constraints used are Poisson's equation,

$$\nabla^2\Phi = 4\pi G(\rho_B + \rho_D) \, , \tag{26}$$

and a velocity moment of the collisionless Boltzmann equation,

$$u^2 - \sigma_R^2\left(\frac{\partial \ln \rho\sigma_R^2}{\partial \ln R} + \beta\right) = R\,\frac{\partial \Phi}{\partial R} \, , \tag{27}$$

which is solved for the bulge and disk separately. These two relations are necessary, but are not sufficient restrictions on the kinematic model. Note that we still have no criteria as to the value or variation of the anisotropy parameters β and β_z. Higher moment equations could supply additional constraints, but these introduce more unknown functions, so we are unable to close the moment equations. Recall that when only two integrals of motion are present, Jeans' theorem requires that $\beta_z = 0$. However, numerical studies show that a third integral is frequently present. Nonetheless, we fit $\beta = \beta_z = 0$ models to our sample of galaxies.

By specifying the form of the off-equatorial plane kinematics (in § III*b*), we have reduced the unknown dynamical structure of the bulge to two functions: $u(R)$, the mean stellar equatorial rotation rate, and $\sigma_R(R)$, the radial dispersion profile. These reductions allow predicted projected profiles to be compared with observed ones. Note that an ambiguity exists because we have constructed a two-component model to be constrained by measurements which combine information from the real both bulge and disk components.

The fitting procedure is as follows. The luminosity density is fitted to the observed photometry; this determines the scale lengths R_e and R_D and the relative surface brightness contributions of the bulge and disk. The bulge R_e, measured along the major axis, is independent of i and ϵ. Since i is determined by the apparent axial ratio of the disk, ϵ can, in principle, be determined by the apparent axial ratio of the bulge. The two scale lengths must be determined by an iterative process; the solution for R_e is particularly sensitive to the disk solution, since small changes in the disk fit at the exterior can extrapolate inward to large changes in the residuals attributed to the bulge. Accurate sky subtraction is necessary for a proper disk solution. Errors up to 25% in R_e exist for those galaxies for which we have only continuum intensity (CI) data. The initial guess for the disk mass is set by fitting the emission-line rotation curve at the outermost measured points; then a rough fit to the bulge mass is approximated by fitting the interior absorption-line data. The potential is computed from ρ_B and ρ_D.

There are two approaches to solving equation (27): (1) an intrinsic mean stellar rotation curve is estimated, initially by scaling up a fit to the observed rotation rate, and σ_R is computed from it by an iterative procedure; (2) a fit is made to the intrinsic velocity dispersion, and the rotation curve computed from it. Either approach will arrive at the same result; the choice is simply a matter of which intrinsic profile is easier to model. Once u and σ_R are derived, they are projected, seeing corrected, and compared to the observed profiles. The seeing profile is chosen to be a single Gaussian, since no better information is available and these corrections are not critical (except for the photometry). A few iterations are required to fine tune the fits. Note that one of the two profiles, $v_{\rm obs}$ or $\sigma_{\rm obs}$, can be made to fit the observations arbitrarily well, perhaps at a sacrifice to the other; the goodness-of-fit must be made by comparing both profiles.

If a satisfactory fit is still not achieved, there are other options to exercise, depending on how the fit needs to be improved; these will be discussed below. We note here that asymmetry observed in the velocity data hints that axisymmetry is an idealization which might improperly restrict the results.

IV. RESULTS

Graphs of the observations and kinematic fits are presented in Figures 3–8. The parameters used in the models are contained in Table 4. Our notation is as follows. The stellar motions are described by their equatorial mean rotation u and velocity dispersion σ_R. The model circular velocity is U_c, the bulge line-of-sight mean rotation is v_s, and the velocity dispersion is σ_s. The predicted observed values, including disk light and seeing effects, are $v_{\rm obs}$ and $\sigma_{\rm obs}$. We refer to the model-projected peak rotation velocity as $v_{\rm peak}$, σ_0 is the central velocity dispersion, and $\bar{v}$ and $\bar{\sigma}$ are the mass-weighted rms values from our models. To compute the means, we have assumed that each spheroidal shell rotates at constant angular velocity and that σ_R is constant along z.

a) NGC 2841

Using the bulge and disk decomposition from Boroson (1981), fits for this galaxy were straightforward, since i, ϵ, R_E, and R_D were already available. The emission-line data were not usable in the observed region; there appears to be an H I hole inside 6 kpc (Bosma 1978). The disk mass was initially set by from a gas-rotation measurement of 260 km s^{-1} at 3.9 kpc by Rubin and Thonnard (1984).

The absorption-line data mostly reflect the bulge; however, a contribution from the disk is expected at the outer observed points. The major axis data are shown in Figure 3*a*, the minor in Figure 3*b*; $v_{\rm peak}/\sigma_0$ is 0.64. The inner peak in the stellar rotation curve is also seen by WRF; although their two sides of

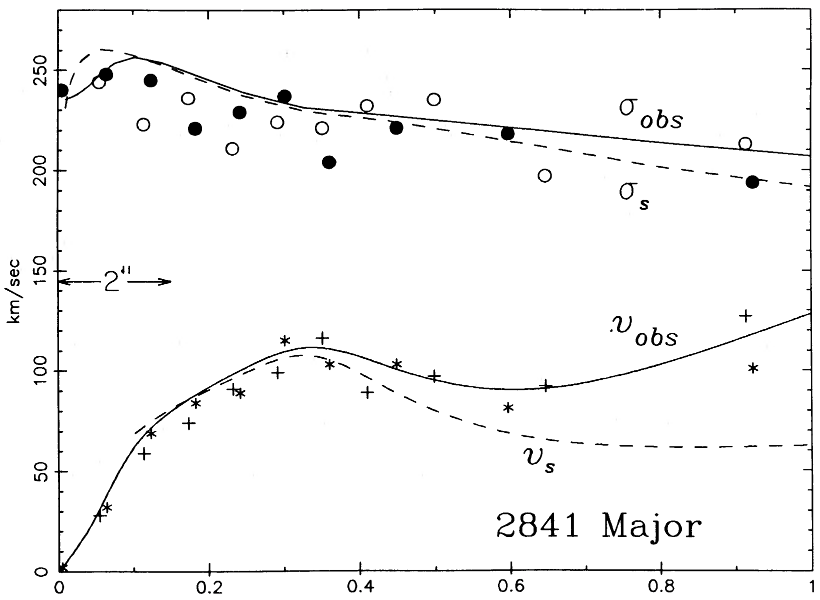

FIG. 3*a*

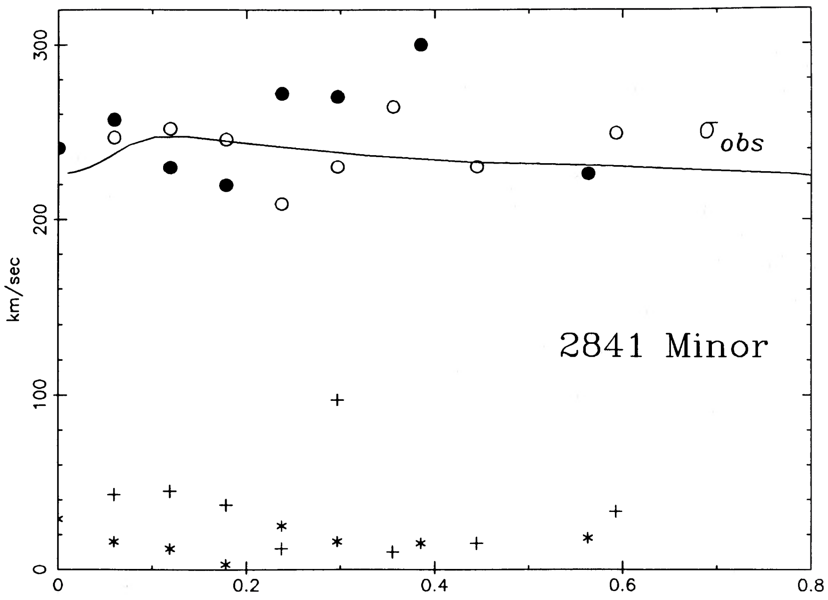

FIG. 3*b*

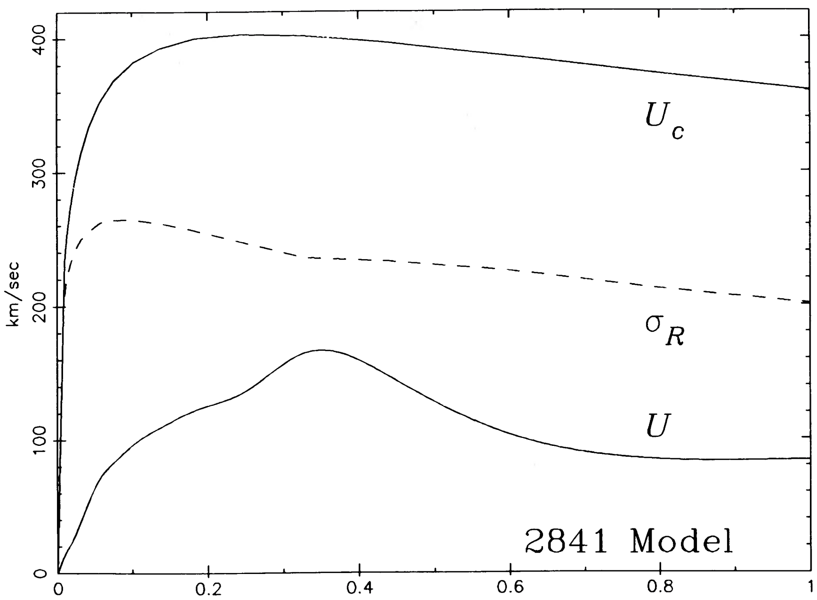

FIG. 3*c*

FIG. 3.—Results for NGC 2841. (*a*) Symbols represent absorption-line mean rotation and velocity dispersion along major axis. Plus signs and open circles (+, ○) for one side, asterisks and filled circles (∗, ●) for other side. Dashed lines are model-projected values for just the bulge, solid lines include disk light and seeing. Arrow labeled in arcseconds illustrates the seeing FWHM. (*b*) Same as (*a*) for the minor axis. (*c*) Model equatorial velocity profiles for NGC 2841. Total (bulge + disk) circular velocity is U_c, the bulge mean rotation is *u*, and its velocity dispersion is σ_R.

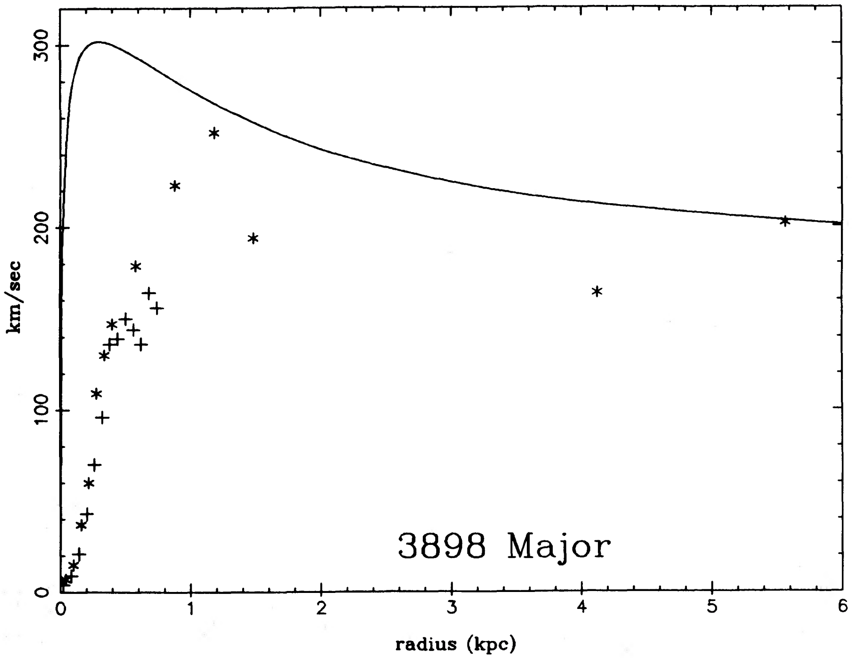

FIG. 4*a*

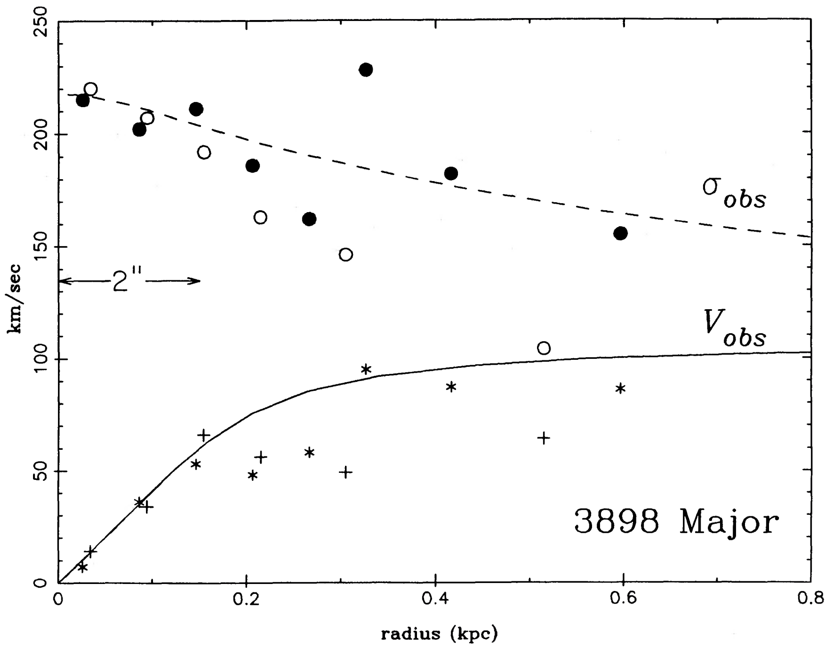

FIG. 4*b*

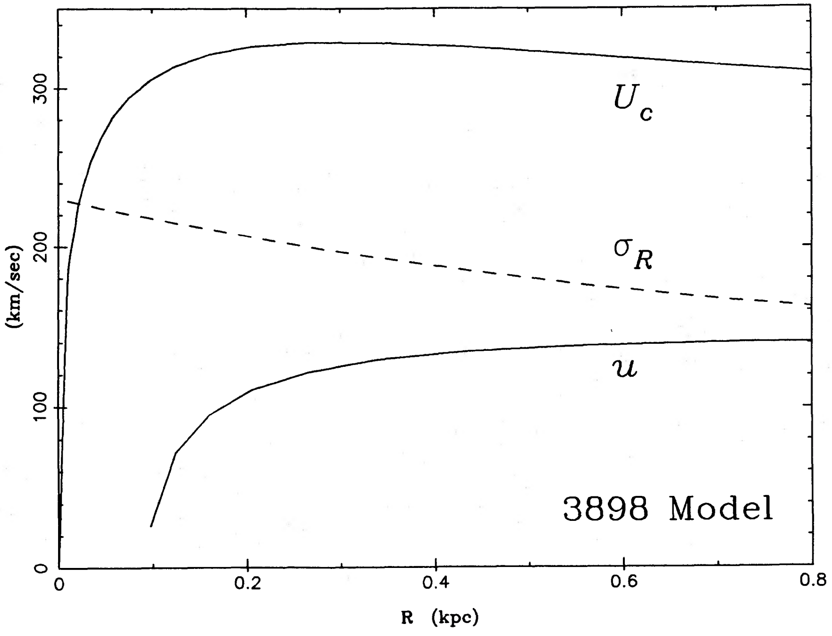

FIG. 4*c*

FIG. 4.—Results for NGC 3898. (*a*) Different symbols distinguish the two sides of the major-axis emission-line rotation curve; solid line is the inclined circular rotation rate. (*b*) Symbols show major axis absorption-line data; both lines represent model values for bulge light only. Arrow labeled in arcseconds illustrates the seeing FWHM. (*c*) Model equatorial velocity profiles for NGC 3898; notation is the same as Fig. 3*c*.

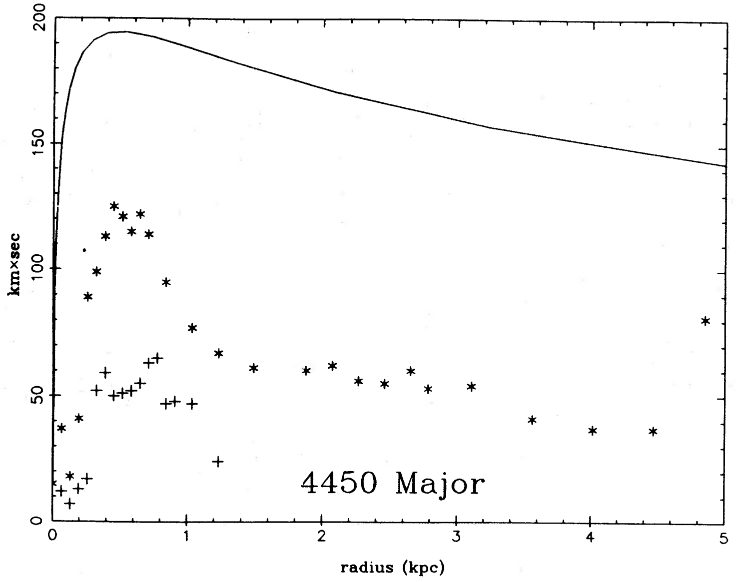

FIG. 5*a*

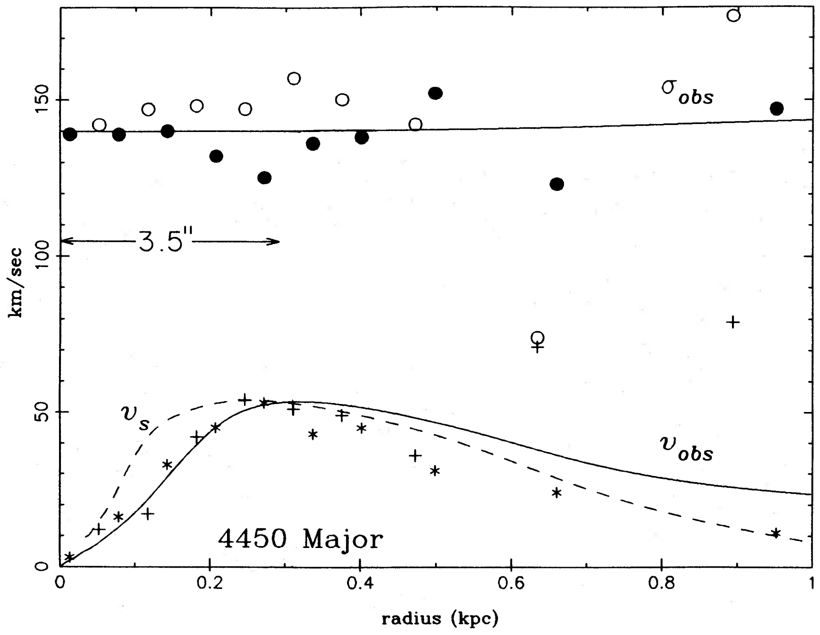

FIG. 5*b*

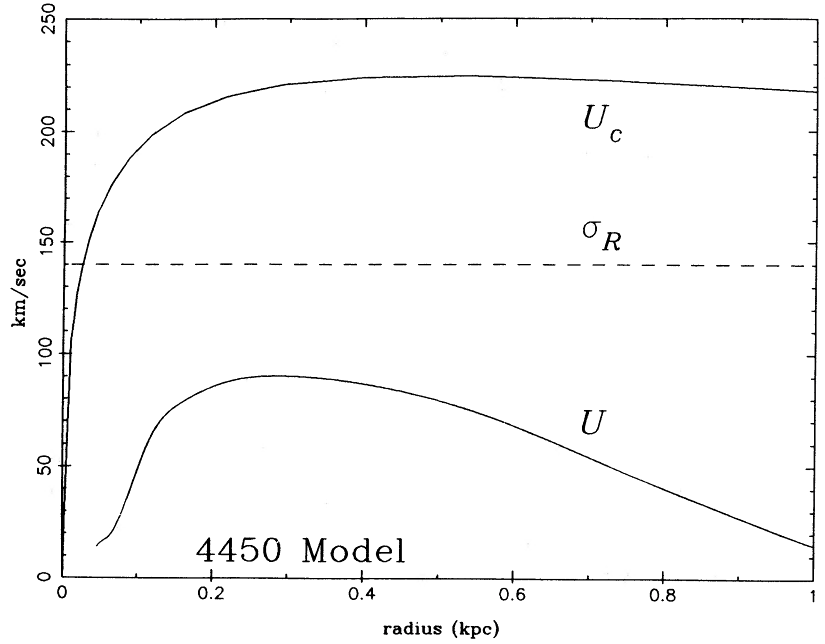

FIG. 5*c*

FIG. 5.—Results for NGC 4450. (*a*) Emission-line data; notation same as Fig. 4*a*. (*b*) Symbols show absorption-line data for two sides of the major axis. Dashed line represents the projected rotation curve for only the bulge; solid line includes both bulge and disk, plus seeing. Arrow labeled in arcseconds illustrates the seeing FWHM. (*c*) Model velocity profile for NGC 4450; see Fig. 3*c*.

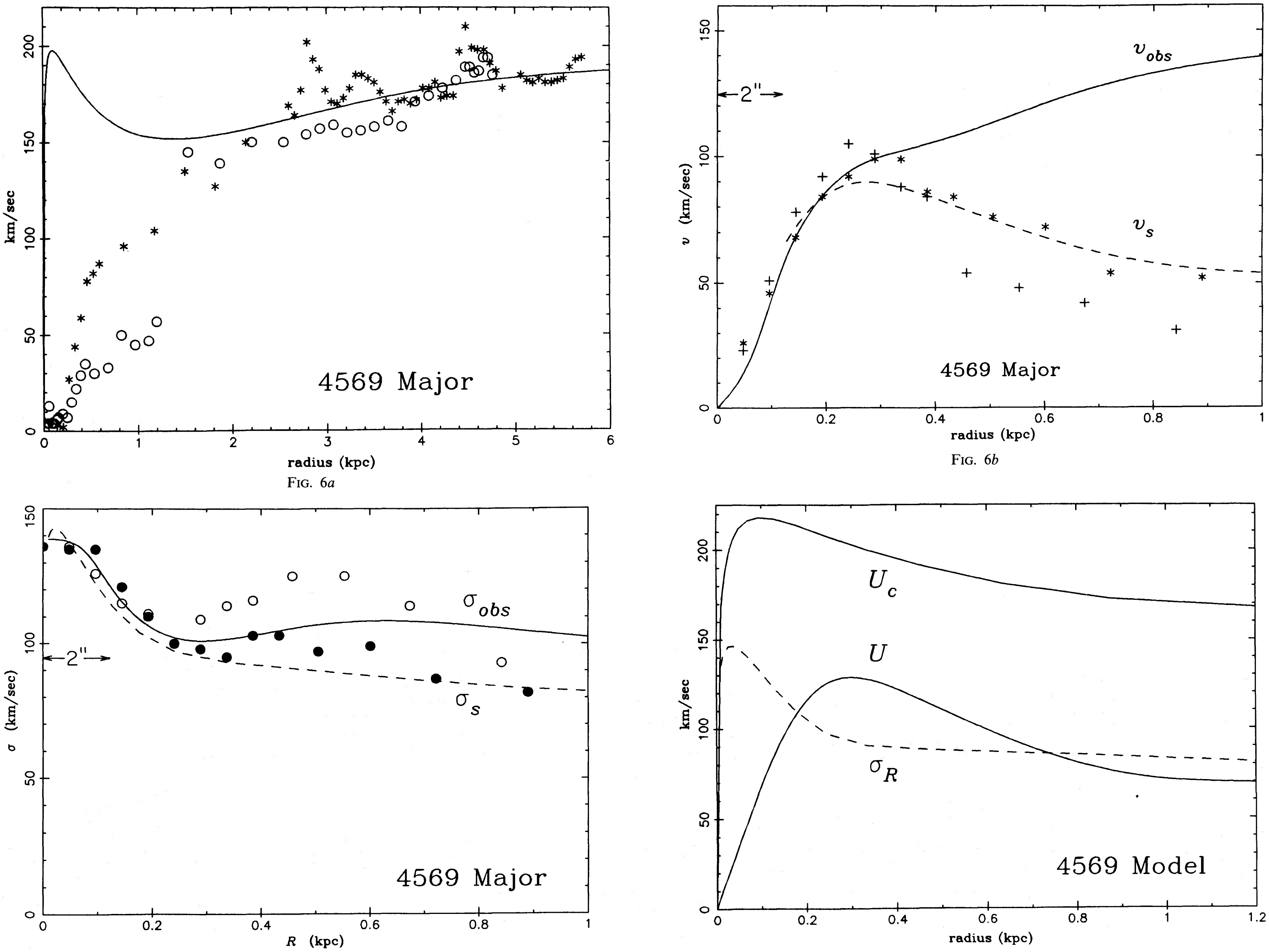

FIG. 6a

FIG. 6b

FIG. 6c

FIG. 6d

FIG. 6.—(*a*) Symbols represent major axis emission-line rotation curve measured in two different years. Solid line is model circular rotation curve. (*b*)–(*c*) Major axis absorption-line data; different symbols represent the two sides of the galaxy; plus signs (+) and open circles (○) from one side, asterisks and filled circles (∗, ●) the other. Dashed lines show bulge only; solid lines include disk and seeing. Arrow labeled in arcweconds illustrates the seeing FWHM. (*b*) Mean rotation; (*c*) velocity dispersion; (*d*) model velocity profiles for NGC 4569; see Fig. 3*c*.

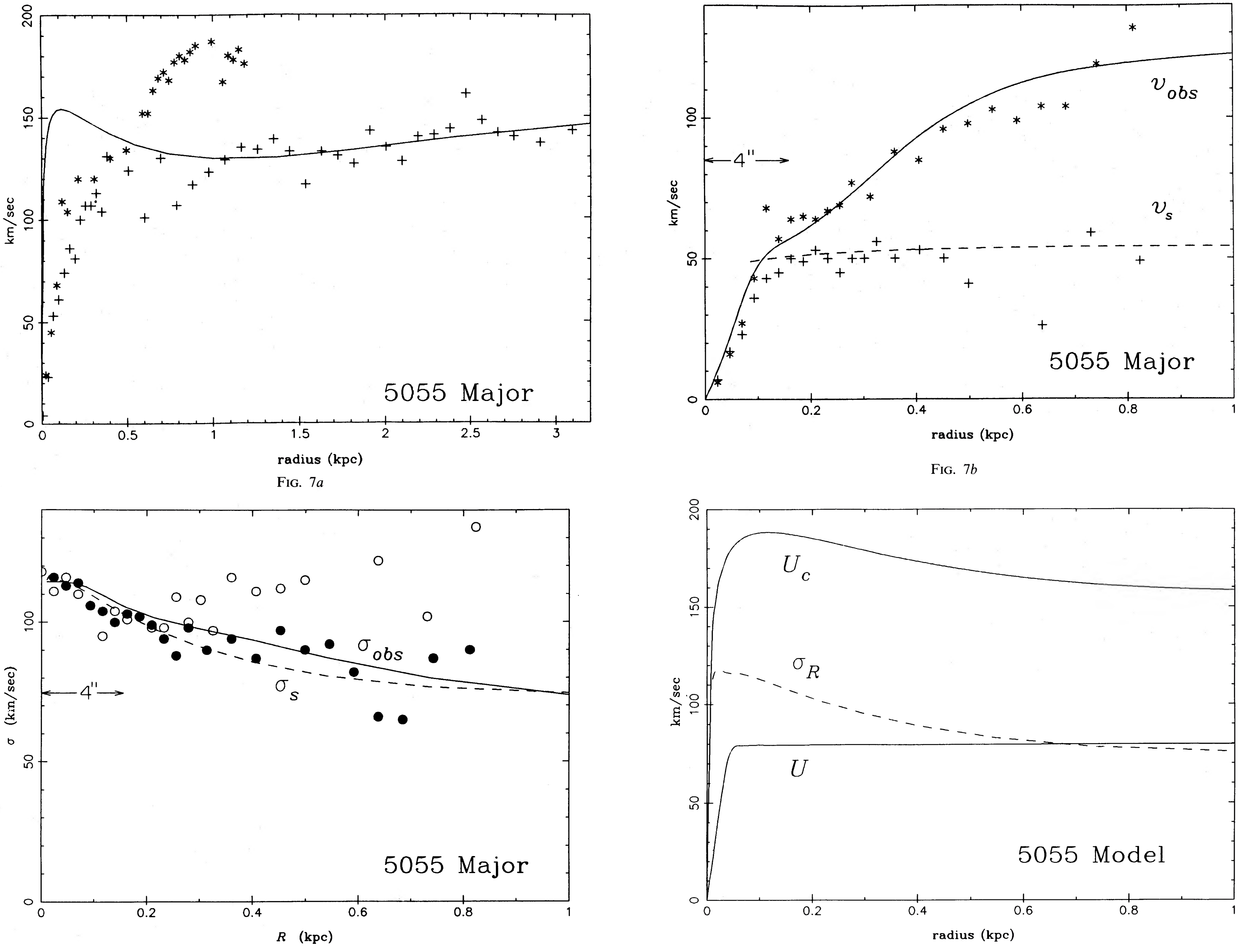

FIG. 7*a*

FIG. 7*b*

FIG. 7*c*

FIG. 7*d*

FIG. 7.—(*a*) Major-axis emission-line rotation curve for NGC 5055, notation same as Fig. 6*a*. (*b*)–(*c*) Absorption-line data, notation same as Fig. 6*b*–6*c*. (*d*) Model profiles, see Fig. 3*c*.

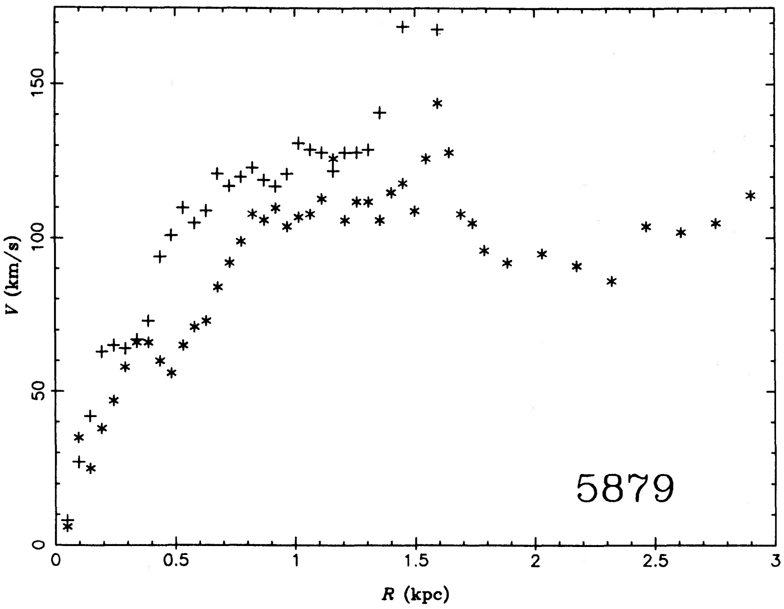

FIG. 8a

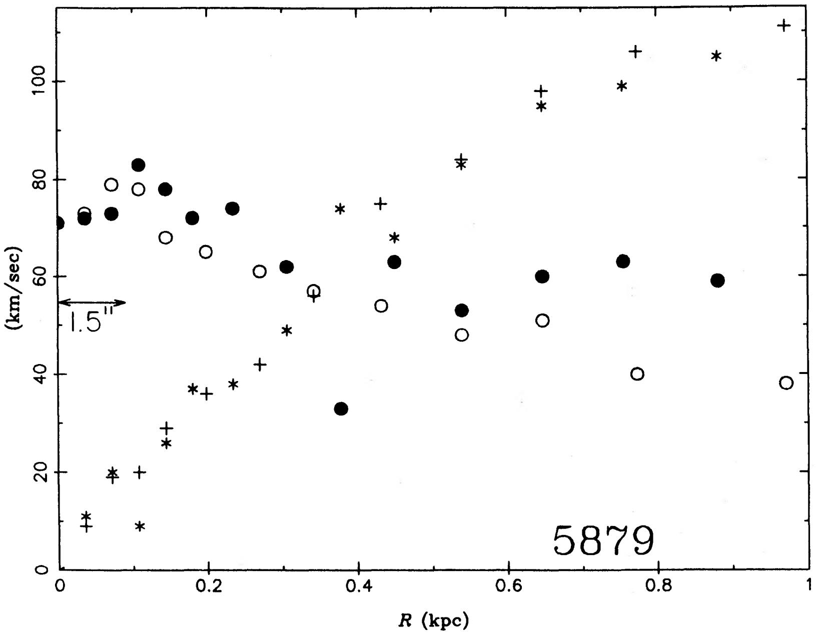

FIG. 8b

FIG. 8.—(*a*) NGC 5879 emission-line rotation curve; different symbols distinguish the two sides of the galaxy. (*b*) NGC 5879 absorption-line data; (+, *) show mean rotation, and (○, ●) show velocity dispersion for each side of the galaxy, respectively. Arrow labeled in arcseconds illustrates the seeing FWHM.

the major axis are not symmetric in the location of the peak, this region is affected by beam bending. Our measured values of the velocity dispersion do not decrease with radius as fast as the WRF values.

The dip in v_{obs} around 0.7 kpc is consistent with equation (27) and the large velocity dispersion. Two different effects could cause the upturn in the rotation curve. If we assume that the observed profiles completely reflect the bulge component, then only a slight decrease in σ_R is necessary to raise the rotation curve; in this case $\bar{v}/\bar{\sigma}$ is 0.70. On the other hand, if the observed rise is due to disk light, then the bulge rotation curve must remain flat to 1 kpc, in which case $\bar{v}/\bar{\sigma}$ is 0.40. This latter interpretation was used for the final model construction because a contribution from the disk is expected, even including the bias of the Fourier quotient method. The model profiles are displayed in Figure 3*c*.

b) *NGC 3898*

The photometry from Boroson (1981) is again used. The observed emission-line rotation data are shown as points in Figure 4*a*; the solid line is the model circular velocity. The major axis absorption-line data are presented in Figure 4*b*. Since the distance where the surface brightness of the bulge equals the disk, which we call the crossover point, is measured

TABLE 4

MODEL PARAMETERS

NGC	Distance (Mpc)	i	ϵ	R_e (kpc)	M_B ($10^9\ M_\odot$)	M_D ($10^9\ M_\odot$)	R_D (kpc)	$\mu_B = \mu_D$ (kpc)	v_p/σ_0	$\bar{v}/\bar{\sigma}$
2841.........	15.7	25°	0.37	0.94	63.0	146	5.4	1.5	0.64	0.40
3898.........	15.8	23	0.33	1.06	44.0	58	4.8	3.5	0.50	0.60
4450.........	17.2	30	0.20	1.70	35.0	13	4.5	1.4	0.45	0.30
4569.........	17.2	25	0.17	0.35	6.8	81	3.6	0.4	0.71	0.70
5055.........	8.2	35	0.28	0.40	5.5	45	2.7	0.3	0.47	0.67

to be 3.5 kpc, while the absorption-line data extend only to 0.6 kpc, we will assume the absorption-line data purely represent the bulge component.

The asymmetry which is seen in both the stellar velocity dispersion and rotation rate is also seen to a similar degree by WRF. The southeast side of the major axis has a rotation rate 30 km s^{-1} lower than the northwest side inside of 8″. The northwest side shows a large decrease in velocity dispersion, whereas the southwest side displays only a slight decrease in our data and a slow rise in the data of WRF.

The model was fitted to the observations by specifying an intrinsic dispersion profile which produced an acceptable $\sigma_{\rm obs}$, and the bulge mass was adjusted until $v_{\rm obs}$ was in the proper range. Note that $\sigma_{\rm obs}$ and $v_{\rm obs}$ fitted well on one side of the galaxy but fitted poorly on the other side. The steep decline in $\sigma_{\rm obs}$ on the poorly fitting side cannot be reproduced without adding a large central mass concentration. However, this addition is tightly constrained by the restriction that the mass of the bulge must not be lowered to compensate for the central mass to the point where $M_B/L_B < M_D/L_D$.

The model profiles are illustrated in Figure 4*c*. The observed $v_{\rm peak}/\sigma_0$ is 0.50; however, $\bar{v}/\bar{\sigma}$ is higher (0.60) since σ_R decreases outward. The model's premature drop to zero rotation velocity inside 0.1 kpc can be corrected by adding $1.6 \times 10^8\ M_\odot$ to the central region, a 14% increase to the mass within 0.1 kpc.

c) NGC 4450

Photometry from Whitmore and Kirshner (1982) was applied in conjunction with our CI data. We compared the apparent scale lengths of the major and minor axis to determine a bulge flattening of $\epsilon = 0.2 \pm 0.2$. The inclination was measured by visual estimates from the Hubble atlas (Sandage 1961). The bulge scale length is uncertain ($R_e \approx 1.7$ to 2.4) because of irregularities in the disk surface brightness, but the best fit to the early turnover in the absorption-line rotation data occurs for a small value of R_e.

The emission-line data are quite irregular, as shown in Figure 5*a*, and the model rotation curve is much higher than the observed one. The high circular velocity of the model is required to fit the absorption-line data, discussed below. This galaxy is unusual in its strong inner peak and the decline of the gas rotation curve inside 5 kpc to below 50 km s^{-1}.

In NGC 4450 the absorption line data extend to 1 kpc (see Fig. 5*b*). The rotation measurements from the two sides agree quite well until 0.5 kpc, then sharply diverge. The two outermost measurements on one side are 50 km s^{-1} higher than the other side, but are still well below the circular velocity, which is over 200 km s^{-1}. By removing the FQ measurement bias, $v_{\rm obs}$ would be high enough to fit the outer observed points, but would now be too far above the inner points. This remarkable asymmetry, if real, cannot be attributed to a FQ bias or a model with a smoothly varying stellar rotation rate. Thus, line-of-sight variations, perhaps because of obscuration by dust, are a likely cause; the surface brightness crossover point is at 1.5 kpc, so the disk contribution is becoming significant. Except for this caveat, a simple model provides a satisfactory fit to the observations. The observed velocity dispersion has a near constant value of 140 km s^{-1} within 1 kpc. The bulge mass was adjusted until the projected bulge rotation profile fit the lower rotation curve (*dashed line*). The disk contribution and seeing effects are included to calculate $v_{\rm obs}$ (*solid line*).

The bulge model profiles are illustrated in Figure 5*c*. Even though $v_{\rm peak}/\sigma_0 \approx 0.45$, $\bar{v}/\bar{\sigma}$ is only 0.30 because u significantly decreases outside 0.4 kpc.

d) NGC 4569

The inclination and bulge ellipticity of NGC 4569 were measured from a CCD picture supplied by G. Bothun. Scale lengths were obtained from fitting major-axis CI data. Figure 6*a* shows the circular velocity fit to the emission-line data. The gas rotation data lie below the model rotation curve out to 2 kpc.

The absorption-line data and fits are presented in Figures 6*b* and 6*c*. The model bulge-rotation curve was fitted to the observations and σ_R derived from it. Projected velocities for the bulge component are shown by dashed lines. The solid lines are computed by combining the line-of-sight bulge and disk velocities weighted by luminosity and corrected for the line-strength bias of the FQ method.

Unlike the observed profile, the predicted $v_{\rm obs}$ does not contain a strong inner peak; because the model bulge-rotation curve fits the observed profile, any inclusion of disk light raises the predicted rotation profile above the observed one. To reduce the model bulge-rotation rate below the observed profile seems even less likely. Evidence for strong absorption is given by asymmetry in the rotation curve and the CI, which differs by 25% from 0.2 to 0.5 kpc. Visual inspection of the galaxy shows abundant dust lanes throughout the inner disk. The observed velocity dispersion profiles are slightly asymmetric, but the predicted profile is roughly consistent with the measured values. The central rise in velocity dispersion is due to the high concentration of the bulge; the contribution from rotational broadening is small. Model profiles for the bulge kinematics are displayed in Figure 6*d*.

e) NGC 5055

The scale-length fits are from the continuum intensity. The surface brightness crossover point is at 0.29 kpc; however, the absorption-line data extend to 0.8 kpc, so we can expect disk light to have a significant effect. First, note in Figure 7*a* that the circular velocity fits the emission-line data on one side of the galaxy quite well. The other side indicates that the gas partakes in noncircular motions since it extends above the model circular rotation curve. Another possibility is that the model should be much higher and something is anomalous with the low-velocity side.

The major-axis absorption-line data are shown in Figures 7*b* and 7*c*. The dashed lines show the projected rotation curve and velocity dispersion for just the bulge component; the solid lines include both bulge and disk contribution. The fact that the bulge-rotation curve fits one side of the observations so well and the bulge-disk combination fits the other suggests significant absorption on the former side (the CI shows an asymmetry of 25%–50% from 0.5 to 1 kpc). The irregularity in the emission-line data supports this hypothesis. Fish (1961) has commented that the "observed isophotes are far from elliptical." If absorption is prevalent, the flat side of the observed rotation curve should be an underestimate of the bulge rotation rate. The ratio $v_{\rm peak}/\sigma_0$ (0.53) underestimates $\bar{v}/\bar{\sigma}$ (0.67) because σ_R decreases from 110 km s^{-1} to under 70 km s^{-1} by 1 kpc ($0.66 M_B$). Using a single-component model, Burbidge, Burbidge, and Prendergast (1960) arrived at a mass 20% below our determination of $51 \times 10^9\ M_\odot$.

The rise in the velocity dispersion on one side of the galaxy is difficult to model. Since the bulge is very concentrated, it is difficult to create a model with an outward-rising velocity dispersion. The average line strengths are lower on the low-rotation side, yet they are expected to be higher if we see more of the bulge on this side. This feature is unexplained at this point.

f) NGC 5879

The continuum intensity for NGC 5879 is too irregular to decompose it into the two components, so the kinematic modeling performed on the other galaxies could not be done for it. Visual inspection indicates a very small bulge; this galaxy is classified as an Sb or Sbc type. The emission-line data are presented in Table 2 and Figure 8*a*; the absorption-line data, in Table 3 and Figure 8*b*. The stellar mean rotation velocity is everywhere the same as the gas. Because the stellar velocity dispersion is small, the observations probably represent solely disk stars. We estimate the disk mass to be $20 \pm 10 \times 10^9\ M_\odot$.

V. DISCUSSION

a) Asymmetries

Several general results of the fitting of the models to the data are interesting. First, we note that the discrepancies between the models and data are often dominated by differences between the two sides of the galaxies. NGC 5055 is a good example of this. Figure 7*a* clearly indicates the ambiguity in deriving the circular velocity from the emission-line rotation curve. Which side (if either) represents the true circular velocity? A similar problem is encountered in the absorption-line data. The same side of the galaxy with higher emission-line velocities has an absorption-line rotation curve which continues to rise to ~120 km s^{-1} outside of 0.1 kpc, while the rotation curve on other side levels off at 50 km s^{-1} at this radius. Furthermore, the higher rotational velocity seems to be allied with a lower stellar dispersion.

Several effects might produce such an apparent difference in the kinematic behavior between the two sides of a galaxy. A real difference in the gravitational potential between the two sides seems unlikely because that would require a mass distribution which is not even bilaterally symmetric. Moreover, one might argue that a local disturbance in the potential is not likely to manifest itself as a simultaneous change in opposite directions of the rotation and dispersion. A more plausible explanation involves variable extinction, which could result in our observing different blends of the kinematic components on the two sides. For example, if dust were distributed throughout a disk whose thickness is small compared to the bulge height, it would principally occult the disk light. If such dust were then asymmetrically distributed in azimuth or existed only on one side of the nucleus, it could account for the apparent asymmetric kinematics we see. Absorbing material is thought to play a role in the observed stellar kinematics near the center of M31 (McElroy 1983; Teuben, Turner, and Schwarzschild 1985). If dust accounts for the observed asymmetry, there is an inherent limitation to our approach until we can measure stellar velocities far enough in the infrared to eliminate extinction uncertainties.

b) What Supports the Gas?

A second interesting feature of several of the spirals is the extent to which the inner part of the emission-line rotation curve falls below the predicted circular velocity. Some of this discrepancy is undoubtedly due to seeing effects; where the velocity gradient is largest, the seeing and the finite slit width will convert some of the change in velocity into an apparent increase in the width of the lines. This effect is confirmed by the emission-line widths, which increase dramatically to widths of 100–150 km s^{-1} at the centers of the galaxies. Outside of 2″–3″, however, the difference between observed gas velocity and predicted circular velocity persists, although seeing effects are negligible. This is particularly apparent in NGC 3898 and NGC 4569.

Variations in M/L are not a solution to this particular discrepancy. The model circular velocities are computed from the observed stellar velocities, assuming isotropic velocity dispersion and that the stellar luminosity density represents only the stellar mass density. The total mass-to-light ratio does not enter into this calculation, so the addition of a massive, dark component would not change the model circular velocity, only the mass attributed to the bulge.

Using this approach, Schechter, Whitmore, and Rubin (private communication) also found emission-line mean velocities lower than expected. However, WRF point out that if the velocity ellipsoid in the bulges is radially elongated, rather than isotropic, then the bulge masses are overestimated. If this were the case, observed velocity-dispersion profiles would be much more centrally peaked. Only the very interior of NGC 3898 displays a gradient sufficient to warrant consideration of largely radial orbits (and it does have the largest discrepancy in the rotation rates). The inner dispersion profile of NGC 4569 would be steeper than is observed if it contained more radial orbits, but seeing effects have reduced the observed gradient so this possibility cannot be ruled out.

We believe that mass overestimates are not the source of the discrepancy, and we consider below several reasons why the gas rotation curve might not represent the true circular velocity. Note that in NGC 4569 the gas mean velocities are below the stellar velocities inside 0.5 kpc.

One possible explanation is that these galaxies have bars oriented in the plane of the sky. As the gas streams along such a bar, its apparent rotational velocity will be less than the circular velocity predicted for an axisymmetric mass distribution. An argument against this is the apparent lack of objects with bars oriented along the line of sight. With the possible exception of NGC 4450, none of the galaxies shows a similar peak rotation velocity at small radii.

A second possibility is that the gas is supported by dispersion rather than by rotation near the center. Again, the line widths support this, although uncertain seeing corrections make a quantitative calculation of the true emission-line widths impossible. If dispersions of 100–150 km s^{-1} do exist in the gas out to 1 kpc, such widths must represent bulk motion rather than thermal velocities.

The similarity between the stellar and gas dispersions suggests a scenario in which the two are related. The idea that the ionized gas in the nuclei of early-type galaxies could result from stellar mass loss, particularly in the form of planetary nebulae, and could be heated by the hot star contribution to the ambient radiation field was first explored by Minkowski and Osterbrock (1959). A modernization of their arguments suggests that such an explanation might indeed be correct. For the amount of gas being returned to the interstellar medium (ISM) by stars we adopt Tinsley's (1980) estimate of 0.02 $M_\odot$ per solar blue luminosity per 10^9 yr at the present epoch. The relevant time to consider is 10^7 yr, since that is the time required for a star to travel 1 kpc at 100 km s^{-1}. That is, we assume that the gas around a star is absorbed by the disk each time that star passes through the disk plane. Thus, there are 2×10^{-4} $M_\odot$ of gas for each solar blue luminosity of stars. This quantity of gas, if ionized, will produce Hα emission amounting to $(4.75 \times 10^{-12})/N_e$ ergs s^{-1} cm^{-2}, where N_e is the electron density in cm^{-3}.

For the electron density we adopt 0.1 cm^{-3}. This is somewhat higher than what might be expected if this amount of gas were uniformly spread throughout the bulge, but is probably more realistic, since we assumed that the large velocity dispersion indicates that the material is still clumpy. Also, this is somewhat lower than the density that a planetary nebula will reach in a few times 10^4 yr, the lifetime of its central star in its hot, luminous phase. The Hα luminosity produced is then 4.75×10^{-11} ergs s^{-1} cm^{-2}. Each solar blue luminosity, emitted by K0 III stars, is accompanied by 6.3×10^{-11} ergs s^{-1} cm^{-2} Å^{-1} at 6500 Å, so the equivalent width produced in Hα is a little less than 1 Å. The observed equivalent widths range from 1 to 3 Å, so we conclude that there is sufficient gas to produce the observed emission.

The second part of the calculation involves the ionizing flux. For this, we use the *IUE* measurements of Oke, Bertola, and Capaccioli (1981) and Bertola, Capaccioli, and Oke (1982) of several bright elliptical galaxies. All of these galaxies show spectral upturns below 2000 Å, which are presumed to be due to either young OB stars or blue horizontal branch stars. Typically, the flux seen in the *IUE* aperture, which corresponds to a region quite similar to the one which we are considering, is equivalent to ~3000 OB stars having a temperature of 30,000 K. For an emission volume V, this ionizing flux corresponds to $N_e^2 V = 3.52 \times 10^7$ pc^3 cm^{-6}, which for our assumed density of 0.1 cm^{-3} is more than sufficient to produce the observed Hα emission.

Although we have shown that what is known about mass loss and the UV contribution to the ambient radiation field is consistent with our explanation for both the origin of the gas and its kinematics, there are two side issues which complicate the argument. First, the time scale for the gas to fall into the disk is 10^7 yr. Thus, one might expect there to be $\sim 10^3$ times as much mass in the gas disk as there is currently falling into it. We assume that this gas cools quickly to a high enough density that the surrounding UV flux can no longer excite it. The gas may be involved in star formation after it has cooled. This process moves material to the center of the galaxy and transports angular momentum outward.

The other issue to consider is why such emission is not seen in elliptical galaxies. After all, they have all the prerequisite properties we have assumed to produce the Hα emission: gas from stellar mass loss and ionizing radiation from the few hot stars. A search of the literature reveals the fact that very few ellipticals have been observed to the accuracy required to detect such emission. A recent survey is described by Caldwell (1984), who has searched for [O II] λ3727 emission in the nuclei of elliptical galaxies. This line is expected to be about a factor of 2 weaker than Hα in H II regions (Hawley 1978), and the stellar continuum is somewhat weaker than at 6500 Å, so the equivalent width of [O II] λ3727 should be about the same as Hα. Caldwell finds that at the few angstrom level, almost half of the ellipticals he has observed show emission. Thus, it might be expected that observations such as ours of the centers of most ellipticals would discover emission-line gas.

c) v/σ and Bulge Flattening

There has been some discussion (see WRF and references therein) of which observed v/σ values best reflect the virial $\bar{v}/\bar{\sigma}$. We have calculated both the model $\bar{v}/\bar{\sigma}$ and the projected $v_{\rm peak}/\sigma_0$. Although $v_{\rm peak}/\sigma_0$ indicates the rough value of $\bar{v}/\bar{\sigma}$, we find that it varies less than $\bar{v}/\bar{\sigma}$ does. The peak values do not sufficiently account for the large variations in either u or σ_R. Thus, if the rotation curve has an inner peak or the velocity dispersion shows a large gradient, modeling the observations to compute $\bar{v}$ and $\bar{\sigma}$ is necessary.

We compare the $\bar{v}/\bar{\sigma}$ value for each galaxy against the virial value assuming isotropic random velocities (Binney 1978, 1980), as presented in Figure 9. We find four of five bulges below the theoretical curve, in general agreement with WRF, who also studied disk galaxies. These results, if significant, suggest that bulges either (1) do not have isotropic velocity dispersions, a result already established for large ellipticals (Davies *et al.* 1983, and references therein), or (2) are additionally flattened by the disk potential. Both effects may be present.

To examine the effect of a disk on each bulge in our sample, we compare our results with some simple theories of bulge flattening by a disk. Monet, Richstone, and Schechter (1981, hereafter MRS) computed the flattening of an isotropic, nonrotating spheroid by a thin disk. Both of their components had scale-free density distributions, so the ratio of bulge-to-disk mass within any isophote is constant, which is unlike our models. The isophotal flattening as a function of $M_B/M_{\rm tot}$ is plotted in Figure 10 as a dashed line. Model fits for our sample are shown as filled circles; three of the galaxies fall near the MRS curve.

An evolutionary approach for estimating disk flattening of bulges has been taken by Barnes and White (1984). They started with nearly isotropic bulges and calculated the effect of the slow accumulation of an exponential disk in the equatorial plane. Since the disk-mass growth rate was slow compared to the bulge dynamical time, the stellar orbits changed adiabatically. Their Figure 5 demonstrates that as the disk mass is

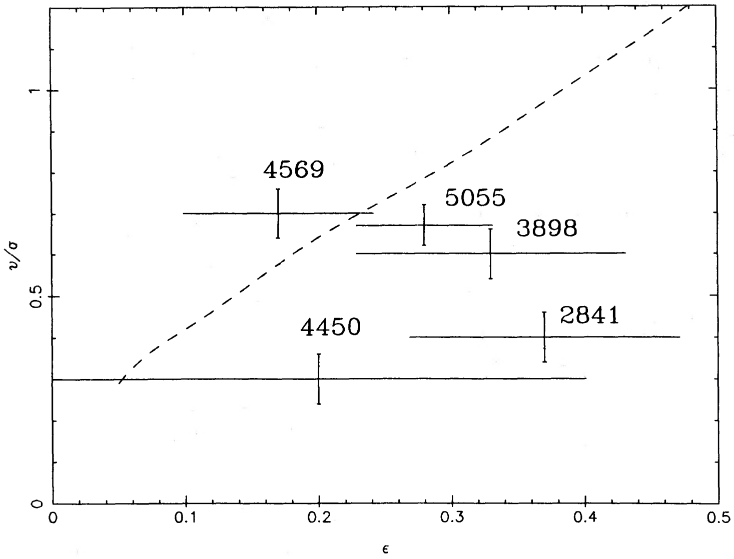

FIG. 9.—Ratio $\bar{v}/\bar{\sigma}$ is calculated from the models for each of the galaxies and measures the relative dynamical importance of rotation. Ellipticity ϵ is based on observations. Dashed line is from Binney (1980) and represents an oblate-spheroidal rotator with isotropic velocity dispersion.

increased, $\bar{v}/\bar{\sigma}$ increases only slightly, whereas the ellipticity increases significantly. Their result for an initially slowly rotating bulge ($\epsilon = 0.25$) is shown as a dotted line in our Figure 10. The flattening of the same three bulges, which are flatter than expected based on $\bar{v}/\bar{\sigma}$, are consistent with flattening caused by the disk. The remaining bulges are very concentrated, so flattening by a disk is expected to be small. To what extent a bulge would remain isotropic while a disk forms within it needs further study.

Thus, we do not refute the conclusion that bulges are isotropic oblate rotators (Kormendy and Illingworth 1982; Dressler and Sandage 1983), but in some cases the disk potential has increased the flattening of the bulge, a conclusion also reached by Jarvis and Freeman (1985). The study by WRF noted that most bulges are below the isotropic $\bar{v}/\bar{\sigma}$ versus ϵ curve but ignored the effect of the disk potential on the bulge shape.

Because our models are not completely self-consistent, we cannot rule out the presence of velocity anisotropies in the bulge. In particular, since the model profiles show significant variation among themselves, it seems unlikely that they all can be isotropic (since the mass models are quite similar). For example, NGC 3898 and 4569 show a large observed velocity dispersion gradient, while NGC 4450 shows no gradient. The addition of our data to the WRF sample weakens their correlation of the dispersion gradient with type (see their Fig. 7).

d) General Implications of the Models

The main conclusion to be drawn from the model fitting is that it is possible to simultaneously fit the surface photometry,

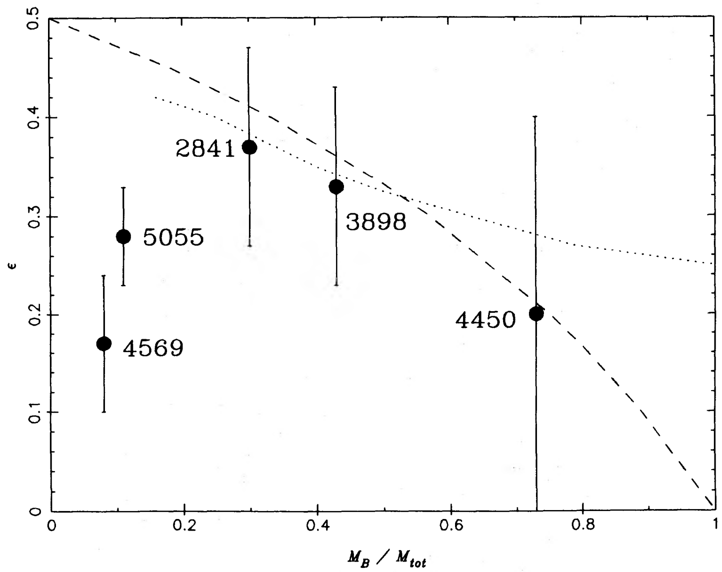

FIG. 10.—Spheroidal bulge flattening caused by a disk as a function of the bulge-to-total mass ratio. Dashed line is taken from Monet, Richstone, and Schechter (1981); dotted line is the result of adding a disk to an initially slowing rotation bulge (Barnes and White 1984).

rotation curve, and dispersion profile of the inner regions of spiral galaxies without recourse to unseen material, central mass concentrations, or even necessarily anisotropic velocity dispersions. We believe that we have identified limitations in both the observational and theoretical aspects of this kind of study. The observations must be more accurate and extend to fainter regions in order to better constrain the models. The presence of unknown amounts of patchy absorption may produce an inherent limitation in studying the kinematics of galaxies, since we may be looking to different line-of-sight depths in different regions.

Another problem is the measurement of the radial velocity and dispersion from a spectrum which consists of a mixture of two populations with different properties. Simulations indicate that the single Gaussian Fourier quotient method is not adequate for this task. Because the region in which the disk and bulge contribute equally to the light is a crucial one for the models, a better technique must be developed for analyzing such data. More general and self-consistent models should be developed, but then, more "unknowns" are required, putting additional burdens on the observations.

To overcome these difficulties, three-dimensional measurements will have to be made: full coverage of a galaxy on the plane of the sky to recognize local obscuration, plus more complete line-profile analysis correlated with intensity variations. This approach will both increase the reliability of the data and supply additional constraints on the models. Only a large observational effort of this sort is ever likely to solve the problem of how galaxies are put together.

Paul Schechter kindly supplied a version of his FQ program for our tests. We thank Alain Porter and Greg Bothun for providing data, Don Schneider for assistance in fitting isophotes, and an anonymous referee for a careful reading of the manuscript and many constructive comments. We appreciate useful discussions with Peter Goldreich, Douglas Richstone, Don Schneider, and John Tonry. This work was supported in part by NSF grant AST 83-13725.

REFERENCES

Bahcall, J. N. 1984, *Ap. J.*, **276**, 156.
Barnes, J., and White, S. D. M. 1984, *M.N.R.A.S.*, **211**, 753.
Bertola, F., Capaccioli, M., and Oke, J. B. 1982, *Ap. J.*, **254**, 494.
Binney, J. 1978, *M.N.R.A.S.*, **183**, 501.
———. 1980, *M.N.R.A.S.*, **190**, 421.
Boroson, T. 1981, *Ap. J. Suppl.*, **46**, 177.
Bosma, A. 1978, Ph.D. thesis, University of Gronigen.
Burbidge, E. M., Burbidge, G. R., and Prendergast, K. H. 1960, *Ap. J.*, **131**, 282.
Burstein, D. 1979, *Ap. J. Suppl.*, **41**, 435.
Caldwell, N. 1984, *Pub. A.S.P.*, **96**, 287.
Davies, R. L., Efstathiou, G., Fall, S. M., Illingworth, G., and Schechter, P. L. 1983, *Ap. J.*, **266**, 41.
de Vaucouleurs, G. 1948, *Ann. d'Ap.*, **11**, 247.
Dressler, A. 1979, *Ap. J.*, **231**, 659.
Dressler, A., and Sandage, A. 1983, *Ap. J.*, **265**, 664.
Fish, R. A. 1961, *Ap. J.*, **134**, 880.
Hawley, S. A. 1978, *Ap. J.*, **224**, 417.
Illingworth, G., and Schechter, P. L. 1982, *Ap. J.*, **256**, 481.
Jarvis, B., and Freeman, K. C. 1985, *Ap. J.*, **295**, 324.
Kormendy, J. 1977, *Ap. J.*, **214**, 359.
Kormendy, J., and Illingworth, G. 1982, *Ap. J.*, **256**, 460.
McElroy, D. B. 1983, *Ap. J.*, **270**, 485.
Minkowski, R., and Osterbrock, D. 1959, *Ap. J.*, **129**, 583.
Monet, D. G., Richstone, D. O., and Schechter, P. L. 1981, *Ap. J.*, **245**, 454.
Oke, J. B., Bertola, F., and Capaccioli, M. 1981, *Ap. J.*, **243**, 453.
Rubin, V. C., and Thonnard, N. 1984, private communication.
Sandage, A. 1961, *The Hubble Atlas of Galaxies* (Washington: Carnegie Institution).
Sandage, A., and Tammann, G. A. 1981, *A Revised Shapley-Ames Catalog of Bright Galaxies* (Washington: Carnegie Institution).
Sargent, W. L. W., Schechter, P. L., and Shortridge, K. 1977, *Ap. J.*, **212**, 326.
Schweizer, F. 1979, *Ap. J.*, **233**, 23.
Seiden, P. E., Schulman, L. S., and Elmegreen, B. G. 1984, *Ap. J.*, **282**, 45.
Teuben, P., Turner, E. L., and Schwarzschild, M. 1985, *Ap. J.*, **289**, 58.
Tinsley, B. M. 1980, *Fund. Cosmic Phys.*, **5**, 287.
Tonry, J. 1984*a*, *Ap. J. (Letters)*, **283**, L27.
———. 1984*b*, personal communication.
van der Kruit, P. C., and Searle, L. 1981*a*, *Astr. Ap.*, **95**, 105.
———. 1981*b*, *Astr. Ap.*, **95**, 116.
———. 1982, *Astr. Ap.*, **110**, 79.
Whitmore, B. C. 1980, *Ap. J.*, **242**, 53.
Whitmore, B. C., and Kirshner, R. P. 1982, *A.J.*, **87**, 500.
Whitmore, B. C., Rubin, V. C., and Ford, W. K., Jr. 1984, *Ap. J.*, **287**, 66.
Young, P. J. 1976, *A.J.*, **81**, 807.
Young, P. J., Sargent, W. L. W., Boksenberg, A., Lynds, C. R., and Hartwick, F. D. A. 1978, *Ap. J.*, **22**, 450.

TODD A. BOROSON and JAMES A. FILLMORE: Department of Astronomy, Dennison Building, University of Michigan, Ann Arbor, MI 48109

ALAN DRESSLER: Mount Wilson and Las Campanas Observatories, 813 Santa Barbara Street., Pasadena, CA 91101